JOURNAL OF GEOPHYSICAL RESEARCH, VOL. 98, NO. A8, PAGES 13,177–13,200, AUGUST 1, 1993

Sizes and Locations of Coronal Mass Ejections: SMM Observations From 1980 and 1984–1989

A. J. HUNDHAUSEN

High Altitude Observatory, National Center for Atmospheric Research, Boulder, Colorado

The SMM coronagraph/polarimeter obtained images of the solar corona in 1980 and from 1984 to 1989. Approximately 1300 coronal mass ejections have been identified in this data set; accurate measurements of angular widths and apparent central latitudes have been made for 1209 of them. The distribution of observed angular widths is broad and slightly skewed toward large values; the average width is 47° (in position angle measured around the limb of the Sun), the median width is 44°. There is no evidence in this data set for any significant or systematic change in angular widths during the epoch of SMM observations. The distribution of apparent central latitudes for all 1209 measurements is roughly symmetric about the heliographic equator, with a root-mean-square average latitude of 35°. The latitude distributions for different calendar years show significant changes in the spread about the equator; mass ejections occurred over a wide range of latitudes at times of high solar activity but were largely confined to near-equatorial latitudes at times of low activity. For example, the root-mean-square average latitude was 41° in 1980, 38° in 1989 (both years near maxima in sunspot number) but only 13° in 1986 (the year of minimum sunspot number). The changes in the distribution of mass ejection latitudes do not correspond to those for solar features or activity related to small-scale magnetic structures such as sunspots, active regions, or Hα flares; they do resemble those of features related to large-scale magnetic structures, such as prominences and bright coronal regions. In 1984, when the "quiet" or background corona suggested the presence of a magnetic dipole structure tilted at ~30° with respect to the solar rotation axis, mass ejection latitudes were clumped about the tilted "heliomagnetic equator" rather than the heliographic equator. Approximately half of the mass ejections that occurred during 1984 were preceded by several days of brightening and spreading of the bright, background corona at the mass ejection site, and produced a conspicuous disruption of the preexisting structure. These observations strengthen the arguments for a close connection between mass ejections and large-scale, closed magnetic structures in the corona.

INTRODUCTION

Coronal mass ejections have been observed both from space and from the ground since the 1970s; for reviews of these observations and their interpretation see *MacQueen* [1980], *Rust et al.* [1980], *Dryer* [1982], *Fisher* [1984], *Hundhausen et al.* [1984*a*], *Wagner* [1984], *Hildner* [1986], *Kahler* [1987*a*, *b*], and *Hundhausen* [1987]. Many questions regarding the nature, origins, and consequences of mass ejections remain unanswered or poorly answered. Among the most interesting of these questions are those pertaining to the origins of the phenomenon. For example, how is this most spectacular manifestation of coronal activity related to more familiar forms of activity, such as solar flares or prominence eruptions, seen in lower regions of the solar atmosphere? How are all of these aspects of activity related to the solar magnetic field? What physical forces drive mass ejections away from the Sun, against the restraining influence of solar gravity; what is the energy source ultimately responsible for their departure from the Sun at speeds ranging from tens to ~2000 km s^{-1}?

A major store of information on coronal mass ejections is the data set obtained with the coronagraph/polarimeter flown on the Solar Maximum Mission (SMM) satellite. This instrument operated from March to September 1980 and (after repair of the spacecraft and instrument) from June 1984 until failure of the satellite pointing system (shortly before reentry into the Earth's atmosphere) in November of 1989. In this 10-year epoch, spanning nearly an entire solar activity cycle, ~240,000 images of the corona were made. Examination of these images has led to identification of ~1300 coronal mass ejections, most of which have been tabulated and briefly described by *St. Cyr and Burkepile* [1990]. We will present an expanded description of SMM results for two basic and easily measured properties of these mass ejections: their sizes and locations. We will summarize the statistical distributions of these properties using the 1209 mass ejections for which good measurements could be made, look for systematic variations over the 10-year epoch of the SMM observations, and compare any such variations with the long-term behavior of other forms of solar activity. We will then examine the results of our analysis in the context of the questions regarding the origins of coronal mass ejections that were outlined above.

Paper number 93JA00157.
0148-0227/93/93JA-00157$05.00

DEFINITIONS AND MEASUREMENTS

The definition of a coronal mass ejection used in examination of the SMM coronagraph/polarimeter data set is that set forth by *Munro et al.* [1979] and restated (with an extension of permissible time scales) by *Hundhausen et al.* [1984*b*, p. 2639], namely "an observable change in coronal structure that (1) occurs on a time scale between a few minutes and several hours and (2) involves the appearance of a new, discrete, bright white-light feature in the coronagraph field of view." The size and location measurements were made as sketched in Figure 1. The locations of the outer edges of the bright feature (at a given distance from Sun center R) can usually be determined to within an uncertainty of a few degrees in the conventional position angle (measured around the Sun, from solar north, in a counterclock-

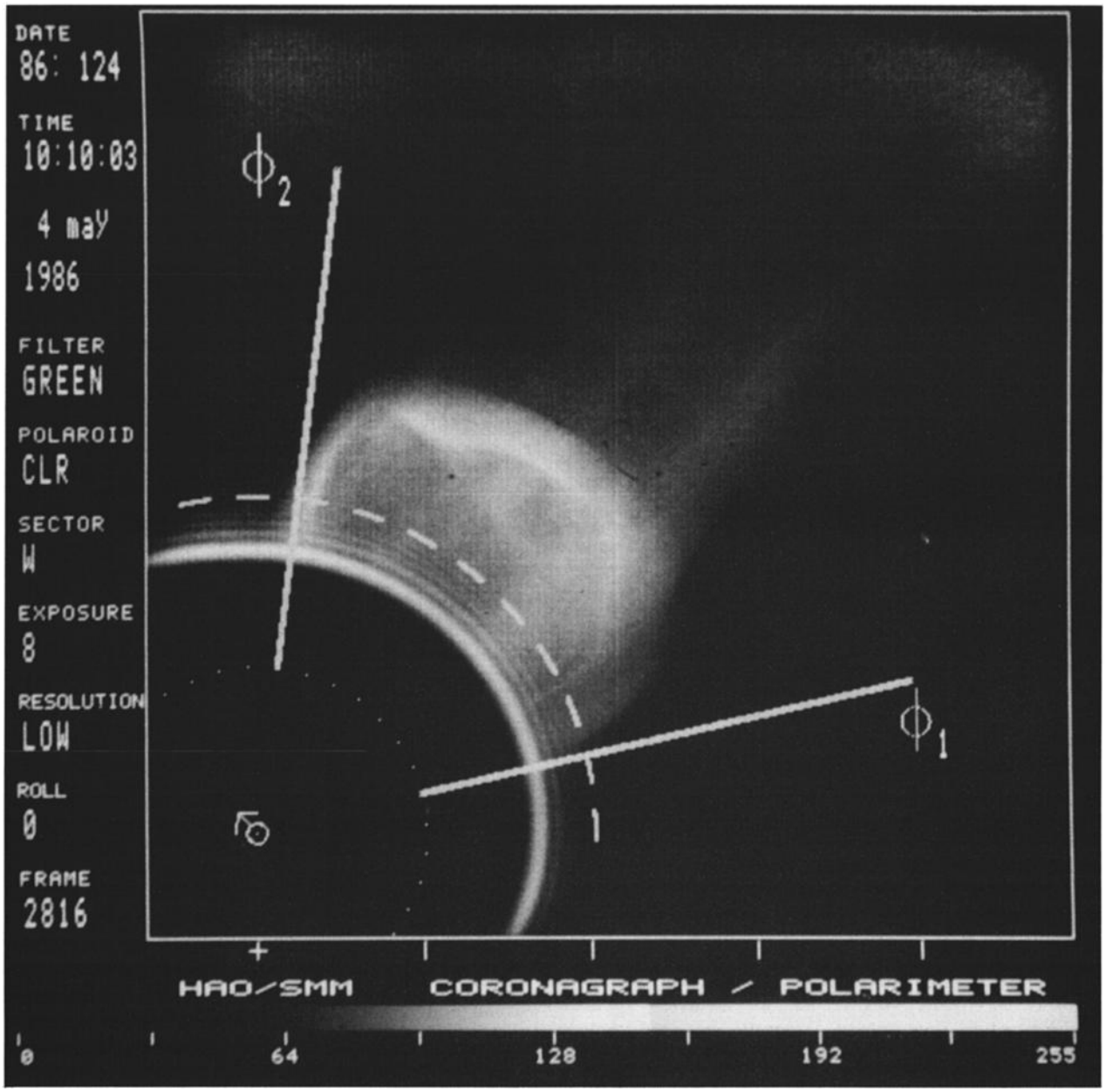

Fig. 1. The definition of the locations ϕ_1 and ϕ_2 for the outside edges of a coronal mass ejection observed by the SMM coronagraph/polarimeter on May 4, 1986. At a distance of 2 solar radii from the center of the Sun, the outer edges of the bright ejected material are at the position angles (measured counterclockwise around the Sun from solar north, indicated by the small arrow at Sun center) $\phi_1 = 240°$ and $\phi_2 = 310°$. Thus the apparent width is $W = 70°$, and the apparent central position angle is $L = 275°$.

wise direction). The apparent width W and central position L of the mass ejection are then defined to be

$$W = \phi_2 - \phi_1$$

$$L = (\phi_2 + \phi_1)/2$$

where ϕ_1 and ϕ_2 are the locations of the two edges. These measurements were possible for 1209 (or 93%) of the mass ejections identified in the SMM data set. Table 1 summarizes the number of ejections with W and L determinations for each calendar year of SMM operations, along with the number of days during each year on which the coronagraph/polarimeter was operated. Because we will be concerned primarily with the origins of mass ejections in this paper, values of W and L at a radius R as close to the Sun as possible will be used; most of these values are from an R of 2 solar radii.

The images on which W and L have been measured were obtained through a filter that transmitted light at wavelengths between 5000 and 5350 Å, or in a broad band in the green region of the visible spectrum. The images thus record a portion of the photospheric light that has been scattered by electrons in the corona. Since the corona is optically thin in this radiation, the brightness at a given point in an image is an integral of the light scattered by electrons along the line of sight passing through that point. This integral is usually dominated by the light scattered from electrons over the limb of the Sun, or near the "plane of the sky" defined as the

plane passing through the center of the Sun, oriented normal to the Sun-satellite line. This dominance stems from the fact that the true heliocentric distance of a point along the line of sight is smallest in the plane of the sky; thus radiation incident on the electrons is highest there. Further, as the coronal electron density is a decreasing function of heliocentric distance, the density of scatterers is normally largest near the plane of the sky. A coronal image in scattered "white-light" is thus a projection of the coronal electron density structure onto an image plane, with the structure near the plane of the sky most heavily weighted in the brightness of the image. The measured widths and locations of coronal features are thus "apparent" in the sense that they are projected on the images. Interpretation in terms of physical sizes or positions is trivial for features near the limb but more subtle for features projected over larger angles. Our initial presentation of statistical results will follow convention and utilize the measured (hence projected) widths and locations. We will estimate the effects of projection of mass ejection locations in a later section where they are compared with the locations of other solar phenomena.

ANGULAR WIDTHS OF CORONAL MASS EJECTIONS

The angular width W is a measure of the size of the region in the corona that is "blown out" in a mass ejection. At a fixed height this region is an area on a spherical surface; W indicates the size of the region projected onto the plane of the sky defined above. The high transparency of the corona in the visible part of the spectrum precludes determination of the size in a direction normal to that plane (or along the line of sight through the corona) using the intensity of scattered radiation.

Figure 2 shows the distribution of mass ejection angular widths (in degrees of position angle) for all 1209 SMM measurements from 1980 through 1989. The distribution is broad and slightly skewed toward large values. The average width of these 1209 ejections is 47° and the median value of the distribution is 44°. Figure 3 shows the distributions of measured widths separately for each calendar year of SMM observations. Each of the seven annual distributions is similar in appearance to that in Figure 2. The average value, median value, and number of measurements for each year are listed in Table 2. All of the annual averages fall within the range 37° to 55°, or within ±10° of the long-term average width. All of the annual median values fall within the range 33° to 50°, or within ±11° of the median value for all measurements. Thus the SMM data do not reveal major variations in mass ejection size over the 7 years of observation. The annual distributions show no major systematic changes and all annual average or median values are within ±25% of the values derived from all data.

TABLE 1. Numbers of Mass Ejections With Measureable Widths and Locations

Year	Number	Days With Observations
1980	159	138
1984	31	197
1985	39	356
1986	44	304
1987	104	277
1988	369	364
1989	463	312

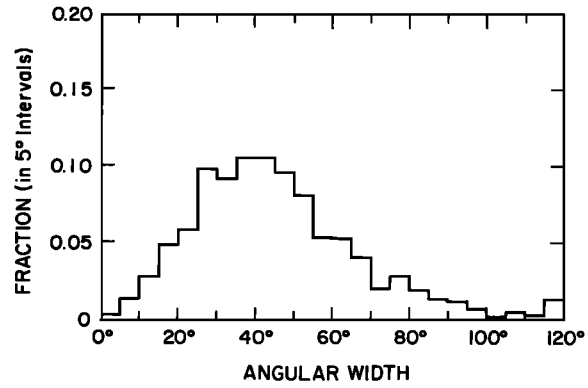

Fig. 2. The distribution of angular widths for 1209 coronal mass ejections observed with the SMM coronagraph/polarimeter. The last bin contains all cases with widths greater than 115°. The average angular width is 47°, the median width 44°.

The absence of any significant variation in mass ejection size may be surprising, as the SMM data set includes observations spanning the full range of solar activity from near-maximum conditions in 1980 and 1989 to near-minimum conditions in 1985 and 1986. Coronal structures and chromospheric conditions are distinctly different in such epochs of high and low activity. The numbers of mass ejections listed in Table 1 (or in Table 1 of *St. Cyr and Burkepile* [1990]) suggest a nearly order of magnitude change in the frequency of mass ejection occurrence. The apparent uniformity of mass ejection size thus suggests a physical structure that is insensitive to many of the changing conditions related to solar activity.

Two other large sets of measured mass ejection widths are appropriate for comparison. E. Hildner (private communication, 1991) obtained the angular widths of 68 mass ejections observed by the *Skylab* coronagraph in 1973 and 1974, or ~2 years before the 1976 minimum in solar activity. The distribution of Skylab widths is shown in Figure 4. The shape of this distribution is similar to those of the SMM distributions in Figures 2 and 3; the average width of 42° deduced from the Skylab measurements is close to the overall average of 47° from SMM observations or the annual averages of 38° and 43° for 1984 and 1985 SMM observations, the years before the 1986 minimum in solar activity. *Howard et al.* [1985, 1986] show distributions of mass ejection widths determined from Solwind coronagraph data for two epochs, 1979–1981 and 1984–1985. Both Solwind distributions are significantly different from the SMM and Skylab distributions in Figures 2–4. The Solwind distributions are much more highly skewed than the others. This difference is reflected in the fact that the Solwind average width for 1979–1981 is 45°, very close to the SMM value for 1980, but that the Solwind median value is in the range (or the bin in the displayed distribution) 5° to 15°, much smaller than the SMM value of 40° for 1980. The average width determined from 1984 to 1985 Solwind observations is 24°, significantly smaller than the SMM averages of 37° and 43° for 1984 and 1985. *Howard et al.* [1986] concluded that the 1984–1985 mass ejections were smaller than those seen in 1979–1981.

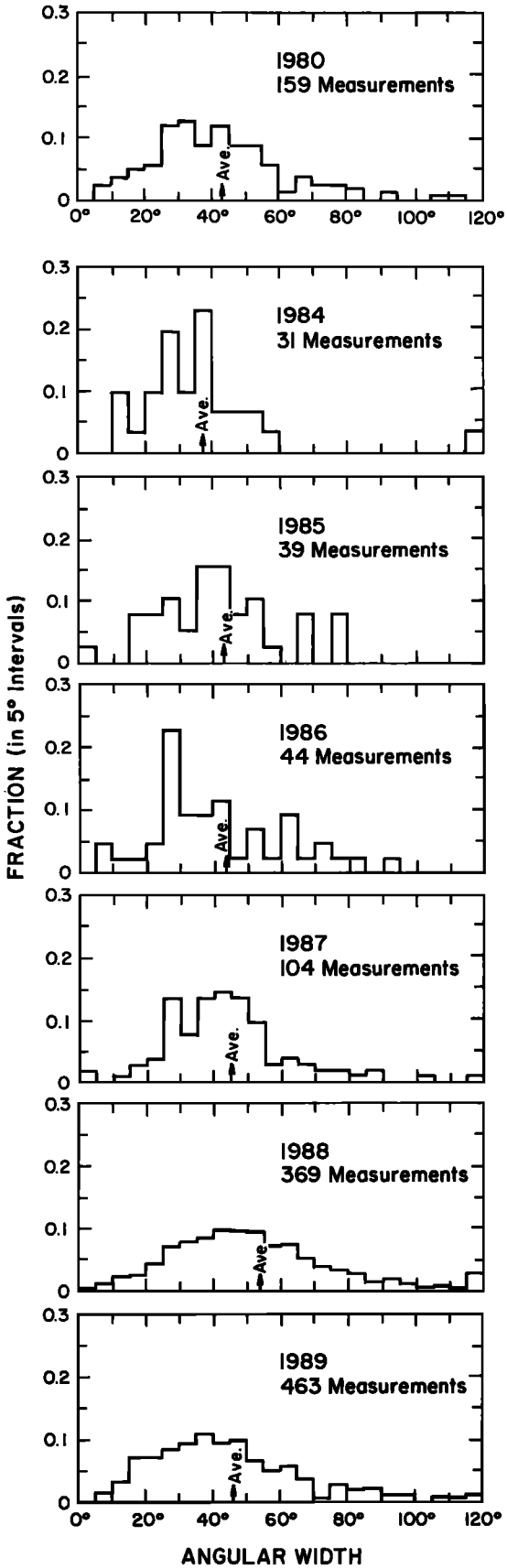

Fig. 3. Distributions of angular widths for the coronal mass ejections observed during each calendar year of SMM operations. Average values are indicated for each year and given, along with medians and numbers of measurements, in Table 2.

TABLE 2. Apparent Widths of Coronal Mass Ejections

Year	Average	Median	Number of Measurements
1980	42.8°	40°	159
1984	37.3°	33°	31
1985	42.8°	40°	39
1986	43.1°	38°	44
1987	45.0°	42°	104
1988	54.1°	50°	369
1989	46.0°	42°	463

The SMM measurements from nearly the same epochs do not confirm a significant difference.

Apparent Latitudes of Coronal Mass Ejections

Interpretation of the central position L of a mass ejection is also complicated by the "projected" nature of the features seen in coronagraph images. The high transparency of the corona in the visible part of the spectrum again precludes determination of location in a direction normal to the plane to the sky (or along the line of sight through the corona) using the intensity of Thomson-scattered radiation. The weighting of regions near the plane of the sky in determining that intensity clearly implies that most observed mass ejections will be near that plane, or above the limb of the Sun. A measured position L is then most easily interpreted as a projected value of the central latitude Λ of the mass ejection. Conversion from the position angle L to a heliographic latitude Λ is trivial and accurate for features near the limb, but subject to increased projection effects with increasing distance from the limb (or the plane of the sky). We will follow convention here and neglect projection effects in converting our measured values of L to values of an "apparent heliographic latitude," displaying distributions of the latter, and comparing them with other measurements of mass ejection locations. However, we will estimate the effects of projection for "off-limb" events when comparisons with the locations of other solar phenomena are made in the following section of this paper.

Figure 5 shows the distribution of the apparent heliographic latitudes measured for all 1209 mass ejections from 1980 through 1989. This distribution is nearly symmetric about the heliographic equator; the average apparent latitude

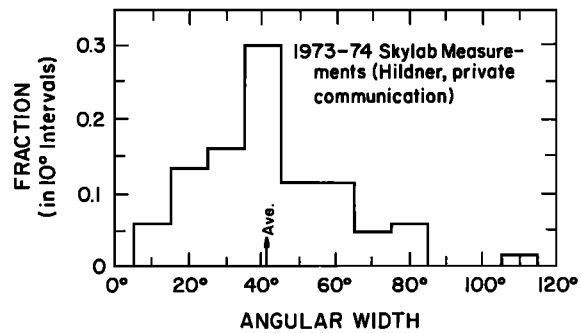

Fig. 4. The distribution of angular widths for 68 coronal mass ejections observed with the Skylab coronagraph in 1973–1974 (E. Hildner, private communication, 1991). The average angular width was 42°.

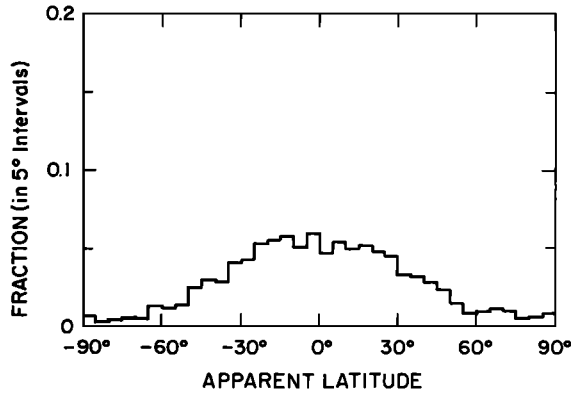

Fig. 5. The distribution of apparent or projected central latitudes (in a heliographic coordinate system) of the 1209 coronal mass ejections observed with the SMM coronagraph/polarimeter.

is 1.5°. While mass ejections have been seen centered at all latitudes, they are most common at low latitudes. The root-mean-square average for all 1209 measurements in Figure 5 is 34.6°. The display of Figure 5 is dominated by the 1015 measurements made during the 3 years of SMM observations when solar activity was high, 1980, 1988, and 1989.

Figure 6 shows the distributions of apparent mass ejection latitudes separately for each calendar year of SMM observations. In contrast to the basic uniformity of the annual distributions of angular widths in Figure 3, there are obvious and significant changes in the annual distributions of apparent latitudes over the SMM epoch. In 1980, near the time of maximum solar activity, mass ejections were broadly distributed in apparent latitude. In 1984, when observations were resumed after the repair of SMM, mass ejections were largely confined to within ±45° of the heliographic equator. In 1985 and 1986, near the time of minimum solar activity, mass ejections were still more confined near the equator; very few ejections were seen at apparent latitudes outside of the range ± 30°. In 1987 and 1988, as solar activity rose toward a new maximum, mass ejection latitudes spread away from the equator to attain, in 1989, a distribution similar to that from 1980. This systematic change can be quantified using annual root-mean-square averages as tabulated in Table 3. This measure of the spread (about an average heliographic latitude that was always within 4° of the solar equator) in the apparent latitude distributions was 41° in 1980, 33° when observations resumed in 1984, reached low values near 13° in the minimum activity years of 1985 and 1986, and then increased monotonically back to 38° in 1989.

The same two other large data sets mentioned with regard to angular widths are available for comparison with these results. *Hildner* [1977] and *Munro et al.* [1979] measured the apparent latitudes of 77 coronal mass ejections observed with the Skylab coronagraph; the distribution of these measurements was shown in an earlier comparison of Skylab and SMM results by *Hundhausen et al.* [1984*b*]. The Skylab distribution, based on measurements from 1973 and 1974, or during the declining phase of a solar activity cycle, is spread over a latitude range of ± 50°. It is thus narrower than the SMM distributions from the maximum activity years of 1980 (as noted by *Hundhausen et al.* [1984*b*]) or 1989 but broader than the SMM distributions from the minimum activity years 1985 and 1986. The Skylab distribution is comparable, but

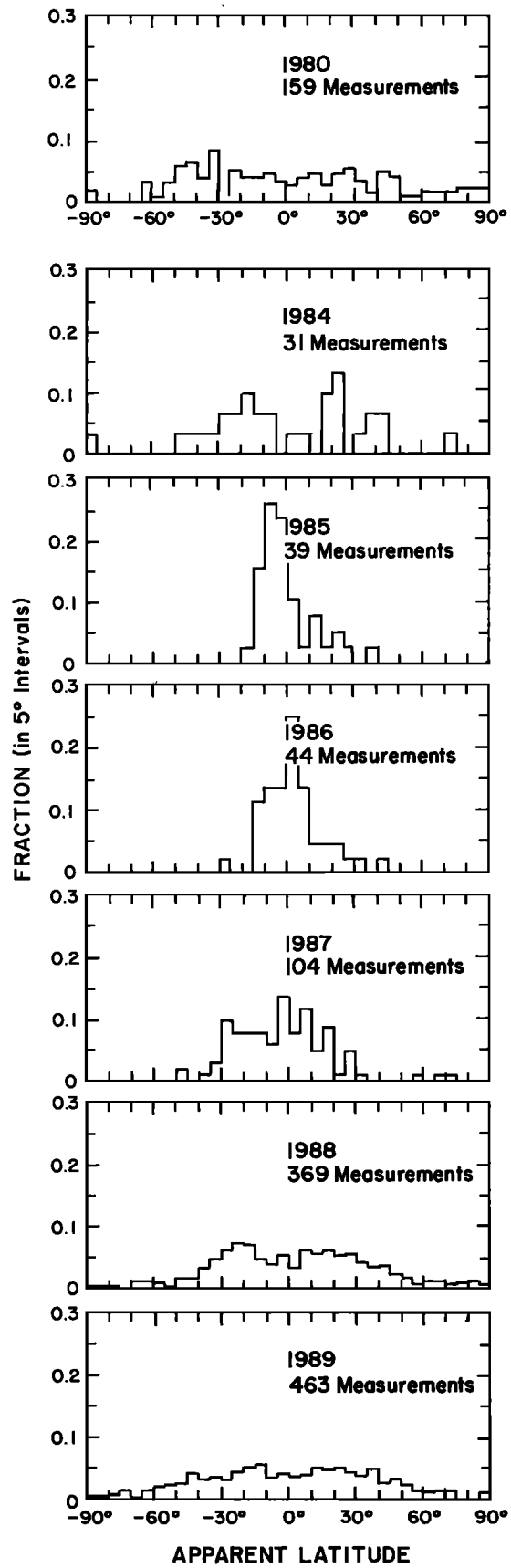

Fig. 6. Distributions of apparent central latitudes for the coronal mass ejections observed during each calendar year of SMM operations.

TABLE 3. Apparent Heliographic Latitudes of Coronal Mass Ejections

Year	Average	Root-Mean-Square Average	Number
1980	−0.7°	41.4°	159
1984	0.4°	33.3°	31
1985	0.8°	12.6°	39
1986	4.1°	13.1°	44
1987	−1.7°	21.4°	104
1988	3.7°	33.1°	369
1989	1.1°	38.3°	463

somewhat more peaked near the solar equator, to the SMM distribution from the "declining phase" year of 1984. The Skylab measurements are thus consistent with the pattern of changing mass ejection locations deduced above from the SMM data set. *Howard et al.* [1985, 1986] show the distributions of central latitudes determined from Solwind observations for the same two periods, 1979–1981 and 1984–1985, mentioned in the previous section. The 1979–1981 Solwind distribution is spread over all solar latitudes and is similar to the SMM distributions for 1980 and 1989 shown in Figure 6. The 1984–1985 Solwind distribution shows mass ejections largely confined to heliographic latitudes between ±45°, roughly consistent with the SMM distributions for those same years shown in Figure 6. The confinement to low latitudes in the later epoch, noted by *Howard et al.* [1986], is consistent with the longer-term pattern of changes suggested by our SMM observations.

Comparisons With Other Solar Phenomena

The pattern of changing mass ejection latitudes during the 1980–1989 epoch of SMM observations invites comparison with the changing locations of other forms of solar activity. For example, one of the best known aspects of the solar activity cycle is the equatorward drift in sunspot latitudes over the ~11 years between successive minima in activity. This effect is often displayed [after *Maunder*, 1922] as a scatterplot of individual sunspot latitudes versus time for one or more activity cycles; the resulting pattern [e.g., *Kiepenheuer*, 1953] is commonly referred to as a "butterfly diagram." We will adopt this same format in displaying and comparing the changing locations of sunspots, active regions, and solar flares (all manifestations of "small-scale" solar activity), prominences and bright coronal features ("larger-scale" features of the solar atmosphere), and coronal mass ejections. The goal of this comparison is, of course, to sharpen our understanding of the relationships among these phenomena.

Despite many studies of these relationships, there is still some disagreement regarding the physical connections of these different manifestations of activity to one another and to the changing magnetic field of the Sun. In particular, there are differing views of the cause-and-effect relationship between coronal mass ejections and two familiar solar phenomena with which mass ejections have often been found to be associated—solar flares and prominence eruptions [see *Rust et al.*, 1980; *Munro et al.*, 1979; *Sheeley et al.*, 1983; *Webb and Hundhausen*, 1987; *St. Cyr and Webb*, 1991] (and see reviews by *Kahler* [1987*a*, *b*], *Hundhausen* [1987], and

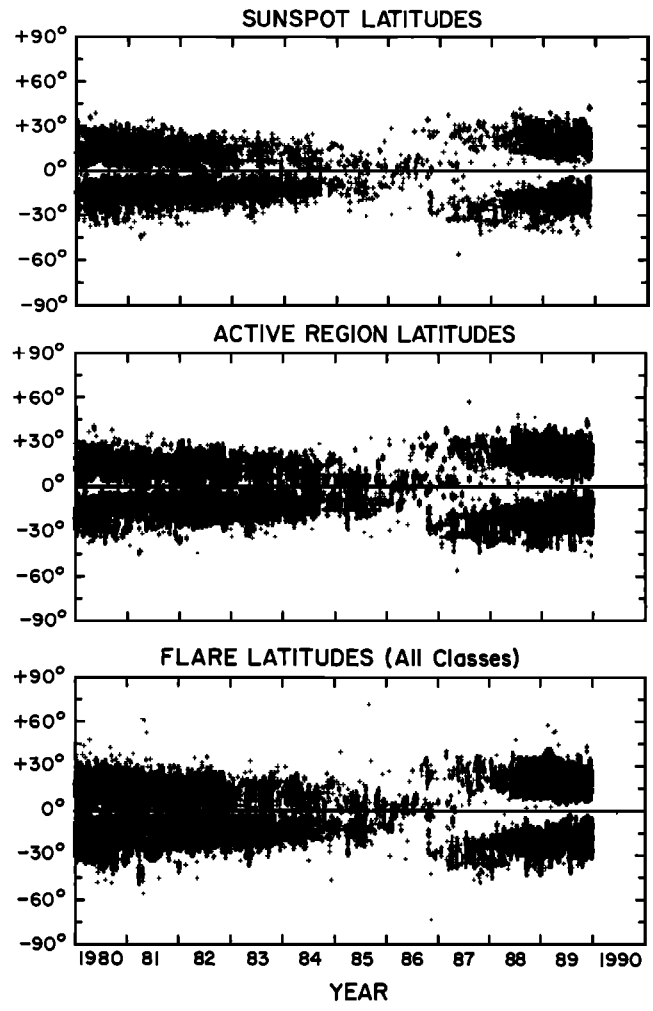

Fig. 7. Scatterplots of the heliographic latitudes of three manifestations of small-scale solar activity (related to small-scale solar magnetic fields) during the 1980–1990 epoch. The top panel shows sunspot latitudes, the middle panel shows active region latitudes, and the bottom panel shows the latitudes of all classes of optical solar flares. All data were provided by the NOAA World Data Center A in Boulder, Colorado.

Harrison [1991*a*, *b*]). The recent interpretation of mass ejections as disruptions of evolving closed magnetic structures in the corona [*Illing and Hundhausen*, 1985, 1986; *Hundhausen*, 1987] suggests the origin of mass ejections in magnetic fields with much larger spatial scales than the fields in active regions or flares [*Harrison*, 1986; *Harrison et al.*, 1990] or even in prominences (see *Low et al.* [1982], *Low and Hundhausen* [1987], and the reviews cited above). Attempts to discriminate among these (and other) suggested relationships on the basis of long-term variations in the rates of occurrence of the different phenomena have been largely inconclusive [e.g., *Webb*, 1991] because these rates for many (or most) forms of solar activity vary in similar ways over the activity cycle. Introduction of the additional information on spatial locations of the phenomena provides an added opportunity to discriminate among these relationships and find new empirical evidence pertaining to the broad questions posed in the Introduction.

The top panel of Figure 7 displays the latitudes of all sunspots in the Mount Wilson/U.S. Air Force/National

Oceanic and Atmospheric Administration (NOAA) listing (obtained from the NOAA World Data Center A), versus time, for the period 1980–1989. This 10-year period covers all SMM observations and spans nearly an entire solar activity cycle from the maximum of 1980, through minimum activity in 1986, to near maximum conditions in late 1989. Because this scatterplot begins near a time of maximum activity, it shows parts of two "butterflies." From 1980 to 1989 a band of spots in each hemisphere migrated toward the equator. In 1986, sunspots related to the new activity cycle appeared at higher latitudes (~30° from the equator) in both hemispheres and produced a second pair of sunspot bands that drifted equatorward through 1989.

There should be no real expectation that sunspots have a direct, physical connection to coronal mass ejections; they have been introduced here as a familiar form of solar activity that illustrates the behavior of solar magnetic field structures on the spatial scales directly related to many well-known types of activity. The middle and bottom panels of Figure 7 display, in the same format, the latitudes of two other familiar solar phenomena, active regions and solar flares observed in Hα, for which there might be some realistic expectation of a close relationship to mass ejections. Both of these phenomena involve magnetic fields with similar (perhaps slightly larger) spatial scales than the fields spreading outward from individual sunspots.

The middle panel of Figure 7 shows the latitudes of all active regions tabulated by NOAA (World Data Center A) for the 1980–1989 period. These regions are the sites of the strong and complex magnetic fields thought to be responsible for the most conspicuous aspects of solar activity. An extremely large active region subtends ~3.5 min of arc as viewed from the Earth [*Allen*, 1973]; the corresponding physical scale is ~2 × 10^8 m or ~1/4 solar radii. The bottom panel of the figure shows the latitudes of all Hα flares tabulated in the same source. Flares are commonly regarded as disruptions of magnetic structures on spatial scales comparable to or smaller than those of active regions.

Both the middle and bottom panels of Figure 7 show a pattern of changing latitudes similar to that in the top panel. This is hardly surprising, as sunspots, active regions, and flares are different manifestations of solar activity on a spatial scale of ≤1/4 of a solar radius; all of these phenomena are thought to be controlled or produced by "small (by comparison with the coronal structures that will be described below) scale" features of the solar magnetic field. It is thus reasonable (and conventional) to ascribe the "butterfly diagram" pattern to magnetic structures that occur with this same spatial scale.

Figure 8 displays, in the same format, the latitudes of two other solar phenomena, prominences and bright coronal features, that have been mentioned as possible sources of coronal mass ejections. The top panel shows the latitudes of dark filaments (prominences seen against the bright solar disk) for the 1980–1989 period. These latitudes were determined from the Hα synoptic maps drawn at the Meudon Observatory and published by NOAA in Solar-Geophysical Data. Latitudes were measured at any place when a dark filament crossed meridians spaced at 13.5° intervals of heliographic longitude (or one day of solar rotation). The measurements should include the locations of most long filaments with some bias toward those oriented in an east-west direction. The typical length of a prominence is ~2 ×

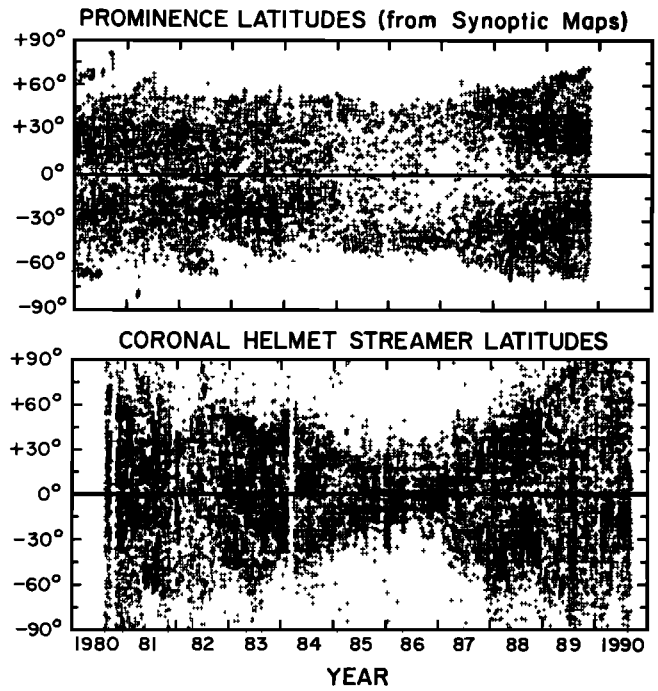

Fig. 8. Scatterplots of the latitudes of two structures related to large-scale solar magnetic fields during the 1980–1990 epoch. The top panel shows the latitudes of prominences shown on Meudon Observatory synoptic maps (see the text for details) and the bottom panel shows the apparent latitudes of bright coronal features seen at the Mauna Loa Observatory.

10^8 m [*Allen*, 1973] or ~0.3 solar radii, greater than the dimensions of most active regions. Prominences are regions of cool, dense (basically chromospheric) material suspended at coronal heights in the vicinity of magnetic neutral lines. They are believed to be supported against solar gravity by a surrounding magnetic field structure with a spatial scale comparable to the prominence length given above.

The spatial distribution of prominences and the long-term evolution of that distribution evident in Figure 8 are both similar to those known from earlier studies [e.g., *d'Azambuja and d'Azambuja*, 1984; *Kiepenheuer*, 1953]; they are strikingly different from those for the smaller-scale manifestations of solar activity displayed in Figure 7. At all times in the 1980–1989 period, the prominences were more broadly distributed in latitude than were sunspots, active regions, or solar flares. Prominences are, in fact, observed to be born near sunspots or active regions and to migrate poleward during the "aging" of the individual active regions wherein they originated (as reviewed by *Kiepenheuer* [1953]). This poleward migration is found to be limited by the location of a so-called "polar crown filament," visible as a relatively sharp, high-latitude limit to the prominence distribution in Figure 8. This location changes systematically over the activity cycle. It moves slowly equatorward during times of decreasing solar activity (1980–1986 on Figure 8) and more rapidly poleward during times of increasing activity (1986–1989 on the figure). During the latter epochs, the distribution of prominences is changing in the opposite sense from that of the smaller-scale activity.

The bottom panel of Figure 8 displays the latitudes of all bright coronal features (defined as any distinct maxima in the coronal polarization brightness observed at a heliocentric

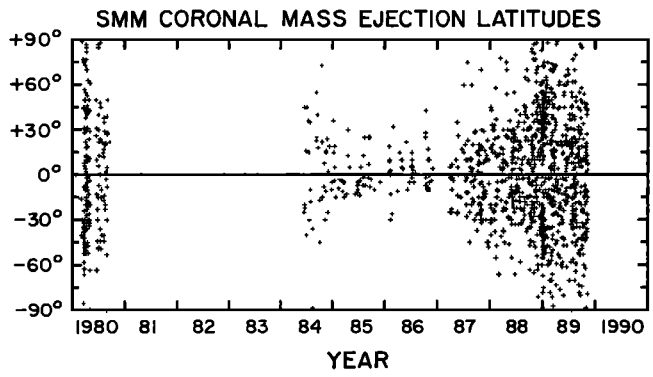

Fig. 9. A scatterplot of the apparent central latitudes of coronal mass ejections observed with the SMM coronagraph/polarimeter.

distance of 1.35 solar radii) measured routinely by observers at the Mauna Loa Observatory from mid-1980 through mid-1990. These bright features usually correspond to the centers of coronal helmet streamers, the same coronal structures seen to be disrupted during the formation of many mass ejections. Helmet streamers are conventionally interpreted as regions of closed magnetic field lines that extend outward as far as a solar radius from the Sun and have horizontal dimensions ranging from $\sim\frac{1}{2}$ to more than one solar radii. Once again, Figure 8 reveals a spatial distribution and a long-term evolution of the distribution that are strikingly different from those for the smaller-scale forms of solar activity in Figure 7. As is well known from photographs of the solar corona obtained during eclipses, bright coronal features are distributed over all latitudes at times of high activity but confined to near equatorial latitudes at times of low activity. The rapid spreading of the distribution of these features visible during the period of increasing solar activity, 1986–1989 in Figure 8, is again a change in the opposite sense from that of the smaller-scale activity.

Finally, Figure 9 shows the apparent central latitudes of coronal mass ejections, determined from the 1980 and the 1984–1989 SMM observations, in the same format used in Figures 7 and 8. The ~40° average apparent or projected width of these mass ejections implies a characteristic physical size (projected onto the solar surface of $\sim\frac{2}{3}$ of a solar radius. The pattern of changes in latitude has already been discussed and need not be described in further detail here. Despite the absence of SMM observations from 1981–1983, it is clear that this pattern differs in one significant way from that of the small-scale phenomena (and presumably small-scale magnetic field structures) in Figure 7. Namely, the poleward spread of mass ejection latitudes during the 1986–1989 period of increasing solar activity is counter to the equatorward drift of the new cycle sunspots, active regions, and related solar flares during that period. For all times away from the epoch of minimum solar activity, mass ejections were seen over an appreciably wider range of heliographic latitudes than the small-scale phenomenon. Given the 40° typical angular widths of mass ejections found above, there is clearly a population of high latitude mass ejections (seen to be centered more than ~50° from the equator) during the years 1980, 1988, and 1989, unlikely to contain spots, active regions, or flares within their angular span.

In contrast, the changing pattern of mass ejection latitudes displayed in Figure 9 bears a much better resemblance to that of prominences and bright coronal features in Figure 8, In particular, the poleward spread of mass ejection latitudes during the 1986–1989 period of increasing solar activity is paralleled by similar trends for both prominences and bright coronal features. Both of the latter occurred over a wide range of latitudes, roughly commensurate with that for mass ejections. In fact, during the period of low activity, 1984–1986, prominences occurred over a wider range of latitudes than did the apparent centers of mass ejections. However, if the typical 40° widths of mass ejections is taken into account, there is no essential inconsistency between the prominence and mass ejection latitude distributions.

Any more detailed discussion of the latitudes of features seen on the solar disk (sunspots, active regions, flares, and prominences) and the apparent latitudes of coronal features seen in "limb observations" requires some consideration of the effects inherent in projecting the latter onto the plane of the sky. A radial feature at true heliographic latitude λ will be seen at the apparent latitude $\Lambda = \lambda$ if it is exactly above the limb of the Sun, but at an apparent latitude $\Lambda > \lambda$ if it is displaced from the limb. In Appendix 1 to this paper we estimate that the visibility of a dense radial structure in the corona is diminished by a factor of two at ~35° from the limb if it is observed in the total intensity of scattered radiation (as in the SMM observations of mass ejections) or at ~25° from the limb if it is observed in the "polarization brightness" of scattered radiation (as in the Mauna Loa observations of bright features). These estimates are consistent with the visibility of near-equatorial rays or streamers for several days as they are carried past the solar limb by solar rotation. Simple geometric considerations (Appendix B) then imply the following conclusions regarding the effects of projection for structures visible within 25° to 35° of the limb.

1. Structures extending radially outward from the latitudes populated by sunspots, active regions, or solar flares will be seen at apparent latitudes Λ only slightly greater than their true latitudes λ. For example, a structure at a latitude $|\lambda| = 30°$, near the maxima in these distributions in 1988 and 1989, would be seen at the apparent latitudes $|\Lambda|$ of 37° when sufficiently far from the limb (35° in the true angular displacement θ) to be seriously diminished in its visibility. Further, a structure with $|\lambda| = 40°$, near the upper limit of the latitudes of these features shown on Figure 7, would never be seen projected to apparent latitudes $|\Lambda|$ greater than 52° if visible as far as 35° from the limb.

2. Structures seen at apparent latitudes $|\Lambda|$ greater than ~60° could have true latitudes $|\lambda|$ anywhere in the range 45° to 90°.

We thus conclude that it is unlikely that the high-latitude mass ejections or coronal bright features on Figures 8 and 9 are the projections of structures at active region latitudes (Figure 7). However, these coronal features could be the projections of structures at the latitudes of prominences in the 50° to 60° latitude range.

In summary, the latitude distributions of the small-scale aspects of solar activity considered above (sunspots, active regions, and flares) are significantly different from the distributions of two large-scale features (prominences and bright coronal features). The distributions of the small and large scale phenomena change in strikingly different ways during part of the activity cycle; while the "active latitudes" wherein spots, active regions, and flares occur drift equatorward during the period of rising solar activity, prominences

and bright coronal features spread poleward during that period. SMM observations from 1986 to 1989, the period of rising activity in the present cycle, reveal a rapid spread in mass ejection latitudes that is consistent with the simultaneous changes in latitudes of the large-scale features and very difficult to reconcile with the changes in latitudes of the small-scale features. Thus our analysis leads to results that are at least consistent with the suggested close, physical relationship of coronal mass ejections with the disruption of large-scale magnetic structures; they are inconsistent with a close, physical relationship with small-scale aspects of solar activity.

A CLOSER LOOK AT OBSERVATIONS FROM 1984

The resumption of SMM operations in 1984, after a hiatus of nearly 4 years, revealed the corona to be in an interesting state intermediate between that expected for maximum and minimum phases of the activity cycle. The "quiet" structure of the corona in 1984 suggested the simple "tilted dipole" configuration seen in the similar "descending phase" of the previous activity cycle [e.g., *Hundhausen*, 1977; *Hundhausen et al.*, 1981]. This structure and its role in organizing the flow and magnetic structure of the solar wind has been described in detail by *Mihalòv et al.* [1990]. We will show here that the locations of coronal mass ejections are also organized with respect to this simple structure of the quiet or background corona, a conclusion that is again consistent with the interpretation of mass ejections as disruptions of large-scale regions of closed magnetic fields in the corona. The structure of the corona is conventionally visualized by means of synoptic maps of the observed brightness [e.g., *Hundhausen et al.*, 1981]. Such maps are constructed by identifying the brightness observed as a function of latitude above one of the limbs of the Sun with the longitude of that limb (thus neglecting any projection effects); a sequence of observations over an entire rotation of the Sun then yields, at any given height, brightness as a function of latitude and longitude. A synoptic map is a plot of the brightness function at the given height in the corona. These maps give a valid description of the distribution of coronal brightness (and by implication the electron density) if that distribution does not change significantly over the 27-day solar rotation period necessary to acquire the data.

Figure 10 shows a pair of synoptic maps based on SMM observations made at a heliocentric distance of 2 solar radii, above both east and west limbs of the Sun, during a single solar rotation in 1984. These and all other maps from 1984 show the basic features expected for a tilted dipole configuration; large regions of low coronal brightness (or coronal holes) in both hemispheres, separated by a more-or-less continuous band of high coronal brightness encircling the Sun as a single sine wave near the equator. This band is conventionally identified [e.g. *Hundhausen*, 1977] with a belt of coronal helmet streamers, permeated by closed magnetic field lines, separating the coronal holes of opposite magnetic polarity in the northern and southern hemispheres of the Sun. The maximum displacements of this belt from the equator (occurring ~180° of longitude apart in the northern and southern hemispheres) indicate a tilt that varies slowly from ~35° in mid-1984 to ~20° at the end of that year [*Mihalov et al.*, 1990].

The location of each mass ejection detected in the SMM data during the same interval of observation is shown on Figure 10 as a white, dashed, vertical line at the longitude of the limb at the time of its detection. The synoptic maps were constructed from the best images (excluding any obtained during a known mass ejection) from each half-day interval of observations. The mass ejection lines are plotted with this same resolution of ~7° in longitude. Their true location in longitude is uncertain by ~35° in light of our conclusion (Appendix A) that a typical ejection is visible over this range of displacements from the solar limb. The vertical extent of each mass ejection line on Figure 10 shows the latitude extent (from ϕ_1 to ϕ_2 in the notation of this paper) of the observed ejection, once again converted to heliographic latitude without correction for any projection effects.

Inclusion of mass ejection locations on the synoptic maps reveals two characteristics pertinent to this discussion. The first of these is rather simple; most of the mass ejections detected in 1984 occurred along the band of high coronal brightness identified with the "magnetic equator" in the tilted dipole system. That is, they emerged above the belt of coronal helmet streamers and closed magnetic field lines that separates the large, near-polar coronal holes. On Figure 10, 8 of the 10 mass ejections detected during the acquisition of data on the maps spanned this belt. Further, both of the remaining mass ejections occurred near secondary bright coronal features that were probably associated with other regions of closed magnetic field lines; the true solar magnetic field is obviously not as simple as a pure dipole. For all of 1984, 27 of 37 detected mass ejections spanned the main band of high coronal brightness. This spatial characteristic of the SMM mass ejections is consistent with other observational evidence (see the summary section) that mass ejections involve the disruption of closed magnetic regions of the corona.

The second characteristic of mass ejections revealed by Figure 10 is more subtle and complicated. An inspection of the maps in the vicinity of the mass ejection lines shows a tendency for the coronal band to be exceptionally bright just to the right of many ejections and exceptionally dim (or almost nonexistent) to the left of the ejections. This characteristic becomes clearer in synoptic maps based on data from greater heights in the corona; Figures 11 and 12 are maps constructed from SMM data at heliocentric distances of 2.8 and 3.4 solar radii obtained during the same solar rotation as in Figure 10. The tilted dipole structure is again evident in these maps, but with the band of bright corona becoming narrower with increasing height (coronal helmet streamers "neck down" to a narrow spike at heliocentric distances beyond ~2.5 solar radii). The brightening and a lateral expansion of this band for 10°–30° in longitude to the right of some mass ejections, and the near disappearance of the band to the left of the mass ejections is more apparent at 2.8 solar radii and very conspicuous at 3.4 solar radii. At the latter height the brightest parts of the coronal band occur just to the right of several mass ejections. The expansion or flaring out in latitude and the sharp disappearance of the bright coronal band gives each of these features the appearance of a "bugle" facing to the left; the entire maps at 3.4 solar radii are dominated by a chorus of bugles emerging from the bright coronal band, each announcing the dawn of a mass ejection.

The key to interpretation of these features lies in the recognition that they reflect a temporal change in coronal

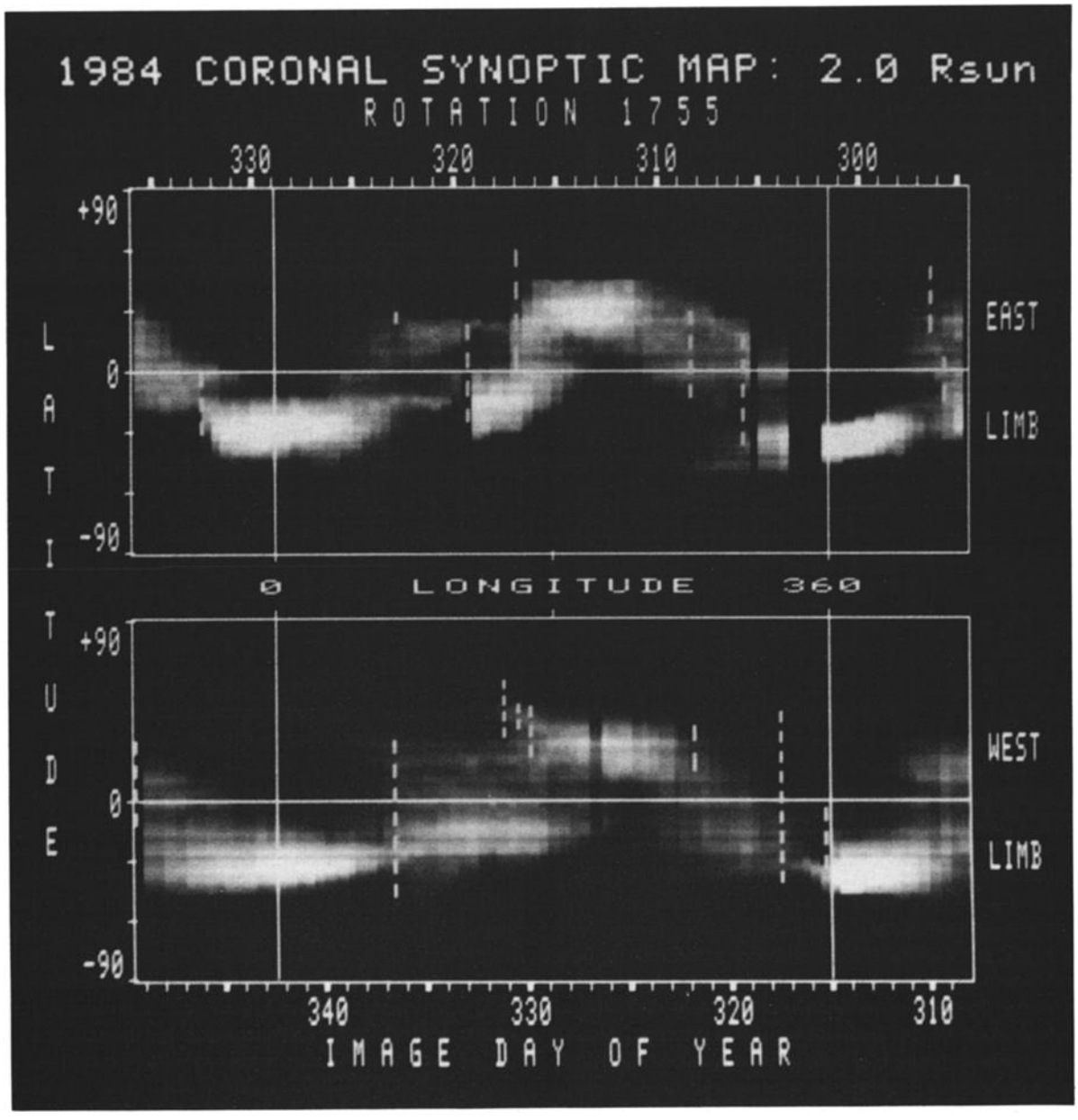

Fig. 10. Synoptic maps of the coronal brightness observed at a heliocentric distance of 2 solar radii during Carrington Rotation 1755 in 1984. SMM observations made over both the east and west limbs of the Sun were used to construct these two maps of brightness as a function of heliographic latitude and Carrington longitude of the limb at the time of observation. The dashed vertical lines represent all coronal mass ejections observed during the same time period. Each ejection is shown at the longitude of the appropriate limb at the time it was observed, extending over the observed range of apparent latitudes.

structure and that, because of the sense of solar rotation, time runs from right to left as data is plotted on a synoptic map. Any spatial feature in the corona, however narrow, would appear to be smeared over the ~±35 deg extent of the scattering function (Appendix A) about the limb. Thus sharper features on these maps stem from temporal changes. In particular, the "bugles" on the synoptic maps represent a brightening and swelling of the bright belt of coronal helmet streamers for several days before the occurrence of a mass ejection and the abrupt disappearance of the bright corona (at least temporarily) after the mass ejection. The swelling and brightening of a large coronal helmet streamer for several days before the mass ejection of August 18, 1980, and the nearly complete expulsion of the material in the streamer by the mass ejection were described by *Illing and Hundhausen* [1986]. This event has been used as the archetype supporting the idea of mass ejections as the consequence of a slow evolution of the closed magnetic fields in a streamer [*Wolfson et al.*, 1987; *Hundhausen*, 1987; *Low*, 1983]. This same behavior is visible in numerous other ejections observed with the SMM and (in retrospect) Skylab coronagraphs. The synoptic maps from 1984 suggest that this can be a common pattern of behavior. The "bugle" pattern is visible for 8 of the 10 mass ejections of Figure 12. Examinations of all SMM synoptic maps from 1984 suggests that this pattern is visible for 19 of the total 37 ejections detected in that year.

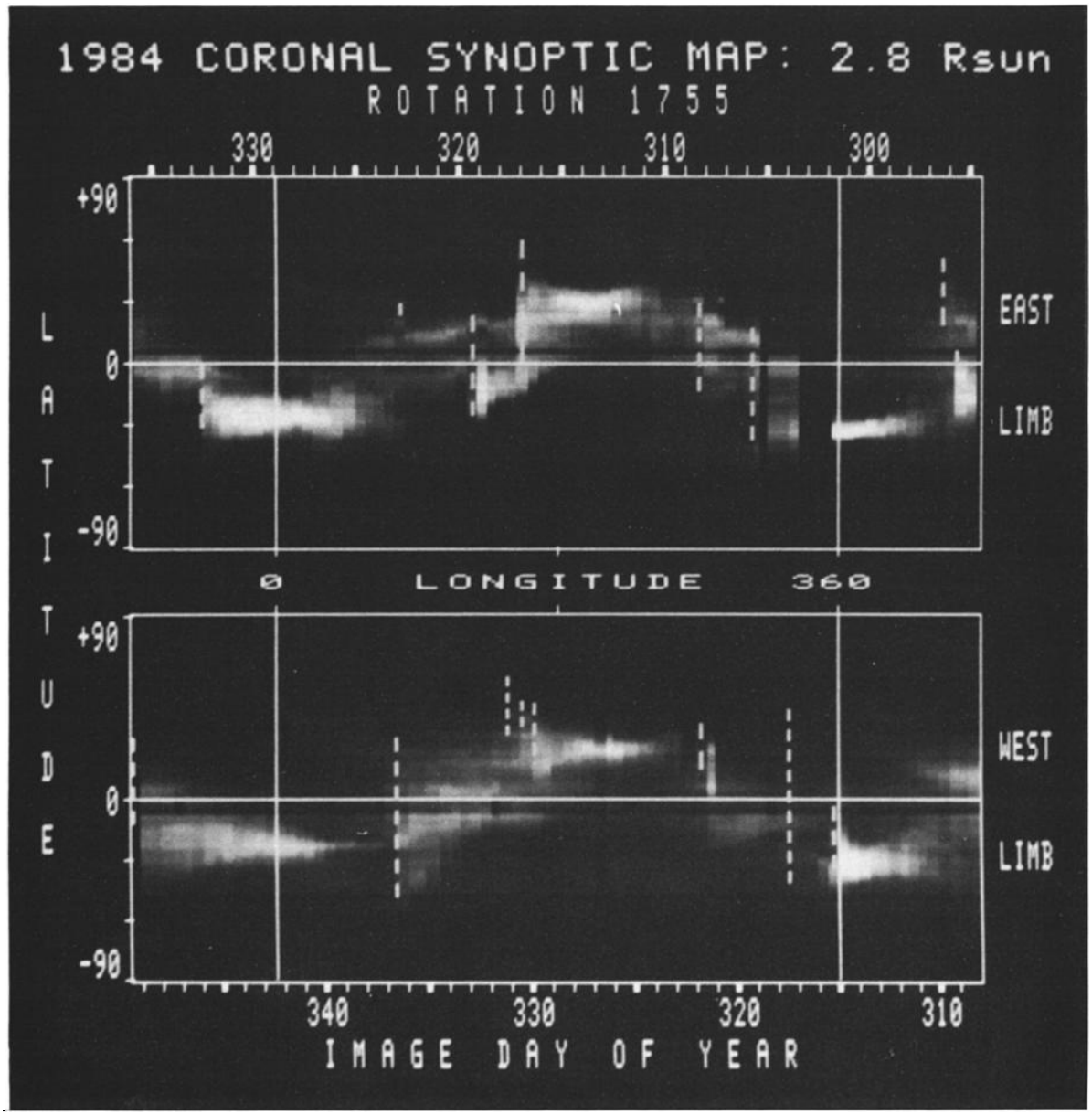

Fig. 11. The synoptic maps for Carrington Rotation 1755 based on SMM observations at a heliocentric distance of 2.8 solar radii.

The occurrence of the bugle pattern for a sizable fraction of the mass ejections observed in 1984 also helps to eliminate the possibility that the mass ejection locations often coincide with the belt of bright corona through some projection effect. This possibility is quite slim on the basis of our visibility analysis in the appendices. All but three of the 32 mass ejection latitudes fall within 45° of the equator; projected latitudes should not be as much as 10° higher than the actual latitudes for these ejections. This possibility is even more unlikely in the light of the changes in the belt associated with the mass ejections. Can we believe that coronal helmet streamers swell in anticipation of and disappear as the result of a projection of effects from some distant location?

Finally, the location of so many mass ejections along the belt of bright corona in 1984 suggests that, like the "quiet" corona and solar wind, this form of coronal activity might be better organized in a "heliomagnetic coordinate system" than in the heliographic coordinates used thus far. In fact, if the quiet corona in 1984 is simply a tilted version of the dipole corona that occurs more nearly aligned with the solar rotation axis in 1985 and 1986 [see *Mihalov et al.*, 1990], display of the distributions of mass ejection locations in the magnetic coordinate system should be a test of the purported relationship of the ejections to the large-scale magnetic structure of the corona. In contrast, the distribution of apparent latitudes shown in Figure 6 for 1984 is not like that for 1985 or 1986; in the heliographic coordinates used in Figure 6, the 1984 mass ejections are spread over a much wider range of latitudes and do not reveal the sharp, near-equatorial maximum evident for 1985 and 1986.

This possibility has been explored by assigning an apparent heliomagnetic latitude Λ_m to 30 of the 31 mass ejections

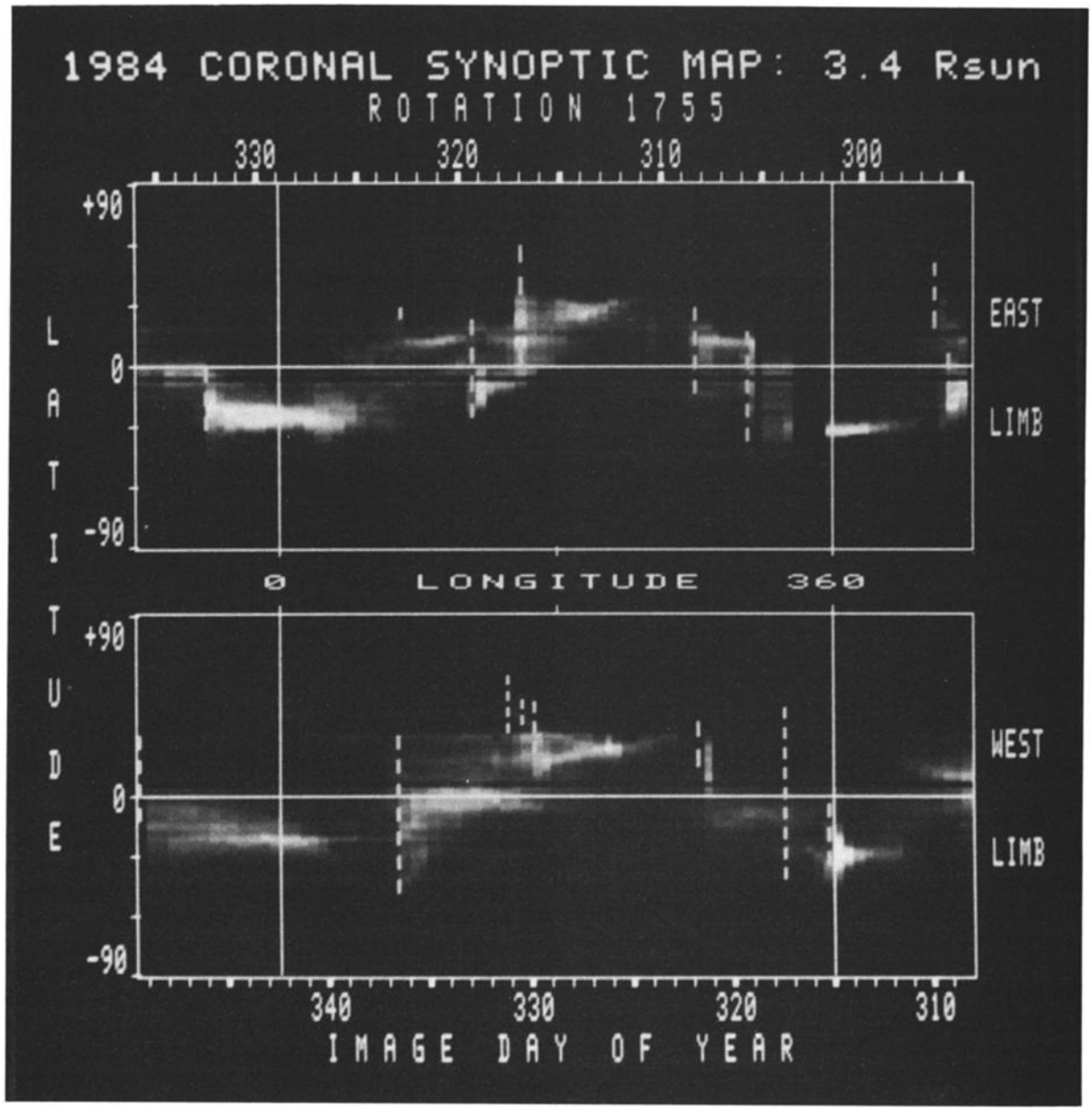

Fig. 12. The synoptic maps for Carrington Rotation 1755 based on SMM observations at a heliocentric distance of 3.4 solar radii.

from 1984. This quantity has been determined by taking the difference of the measured heliographic central latitude for each ejection and the heliographic latitude for the brightest part of the continuous band of bright corona at the same longitude. The distribution of apparent latitudes in the heliographic (as in Figure 6) and heliomagnetic coordinates are shown in Figure 13. It is clear that transformation to a heliomagnetic coordinate system has produced a much narrower, sharply peaked distribution of mass ejection latitudes; the root-mean-square deviation is reduced from 33° to 21° The new distribution closely resembles those from 1985 and 1986 when the two coordinate systems were little different. This result is again consistent with suggestions that coronal mass ejections are closely related to the large-scale, closed magnetic structures that extend into the solar corona.

SUMMARY

We presented a statistical description of the sizes and locations of 1209 mass ejections observed with the SMM coronagraph/polarimeter in 1980 and 1984–1989. The average width of the coronal mass ejections detected with this instrument was close to 40° in angle for the entire epoch of SMM observations; there is no evidence for a significant change in mass ejection widths as reported by *Howard et al.* [1986]. In contrast, there is clear evidence for changes in the latitude distribution of mass ejections over this epoch. Mass ejections occurred over a much wider range of latitudes at the times of high solar activity (1980 and 1989) than at times of low activity (1985–1986). These changes were consistent with the well-known pattern of activity cycle variations in

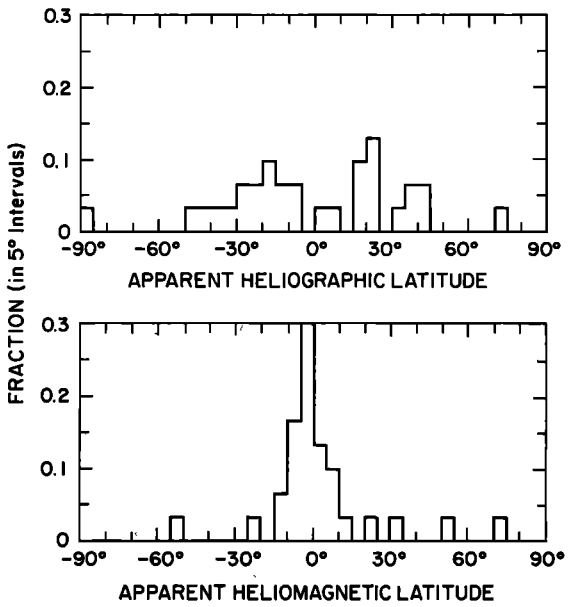

Fig. 13. The distributions of coronal mass ejection latitudes from 1984, shown in (top) heliographic and (bottom) heliomagnetic coordinate systems.

the "quiet" corona and with earlier suggestions [*Hundhausen et al.*, 1984*b*; *Howard et al.*, 1986] based on data sets covering a much smaller fraction of an activity cycle.

Further analysis of the latitudes of the mass ejections observed with the SMM instrument yields several pieces of evidence consistent with a strong relationship to large-scale structures in the solar magnetic field. In particular, the rapid spread in mass ejection latitudes during the 1987–1989 period of rising solar activity occurred while such small-scale manifestations of activity (and magnetic fields) as sunspots, active regions, or flares were slowly drifting equatorward. However, both prominences and bright features in the "quiet" corona (both related to large-scale magnetic fields) spread to high latitudes during 1987–1989 in a manner consistent with the behavior of the mass ejections. In 1984, when the quiet corona has assumed a spatial configuration interpretable in terms of a tilted-dipole magnetic structure, the observed mass ejections tended to occur near the tilted heliomagnetic equator and often involved a preevent swelling and postevent disruption of the helmet streamers in this configuration. In fact, a majority of the mass ejections observed with the SMM coronagraph in 1984 appeared to emanate from bright regions of the corona where the magnetic field is thought to be largely closed.

Much observational evidence relating mass ejections to the evolution of large-scale features (and magnetic fields) in the corona has accumulated over the past decade. Detailed examinations of individual mass ejections provided the first evidence that their formation was a part of a longer-term evolution of closed magnetic structures within a coronal helmet streamer [*Fisher et al.*, 1981; *Low et al.*, 1982; *Illing and Hundhausen*, 1985, 1986; *Low and Hundhausen*, 1987]. Simple theoretical models [*Low et al.*, 1982; *Wolfson*, 1982, 1986; *Wolfson et al.*, 1987] and further discussion of individual ejections (e.g., the reviews by *Low* [1986], *Hundhausen* [1987], *Kahler* [1987*b*], and *Steinolfson* [1990]) and related prominence eruptions [*Kahler et al.*, 1988] have lent plausibility and some credibility to the view that slow evolution of a large-scale, closed magnetic structure can lead to the catastrophic onset of a mass ejection and disruption (at least temporarily) of the original magnetic structure. This possibility (and the related eruption of a prominence and surrounding closed magnetic fields) has been extensively explored in recent papers, sometimes in the context of observations [e.g., *Forbes*, 1990; *Martins and Kuin*, 1989; *Steinolfson*, 1991], and sometimes in considerable isolation from the observational or early theoretical frames of reference [e.g., *Klimchuk*, 1990; *Mikic et al.*, 1988; *Priest*, 1988; *Sturrock*, 1991]. The latitude distributions of mass ejections reported in earlier studies [*Hundhausen et al.*, 1984*b*; *Howard et al.*, 1985, 1986] were consistent with emanation of the ejections from the latitudes of bright coronal rays or streamers. *Howard et al.* [1985] and *Sheeley et al.* [1986] proposed a distinct class of "streamer blowout" mass ejections that had low speeds and occurred at a nearly constant rate in 1979–1985. The evidence presented here relating mass ejections to coronal streamers and rays (or magnetically closed regions), covering a large fraction of an activity cycle, including ejections with no selection of speeds, and involving the preevent "swelling" of streamers, is the most extensive available statistical basis for the concepts described above.

However, this evidence (and that of *Harrison* [1990]) is inconsistent with a conclusion regarding the origin of coronal mass ejections that has been drawn by *Hewish et al.* [1985], *Hewish and Bravo* [1986], and others. These authors traced time-dependent density disturbances or "erupting streams" observed in the solar wind back to an origin in coronal holes. *Hewish and Bravo* [1986, p. 199] suggest "that CME's [coronal mass ejections] are manifestations of erupting streams closer to the sun" and conclude (p. 197) "that CME's should also be associated with coronal holes." Such an association is not found in this study; rather we have found several lines of evidence, none of which require a long and difficult extrapolation from interplanetary space back to the Sun, that mass ejections are commonly associated with the physical antithesis of coronal holes, namely coronal regions where the magnetic fields are predominantly closed and from which the steady solar wind does not emerge.

APPENDIX A: VISIBILITY OF CORONAL FEATURES AWAY FROM THE SOLAR LIMB

As outlined in the Definitions and Measurements section of this text, the brightness or intensity of the corona observed by the SMM coronagraph at a given coordinate in a coronal image is essentially the sum of the light scattered into the instrument by electrons along the "line of sight" passing through the corona at that coordinate. The sum or integral is usually dominated by contributions from the region where the line of sight is closest to the Sun because both the intensity of photospheric radiation and the density of scattering electrons are highest in that region. The scattering process is sufficiently simple that this effect is easily analyzed; with a few simplifying assumptions as to the properties of photospheric radiation and the geometry of a coronal density structure (such as a mass ejection or a bright ray), changes in the visibility of these features with displacement from the solar limb can be quantified. We will describe such a quantification here for coronal features observed in

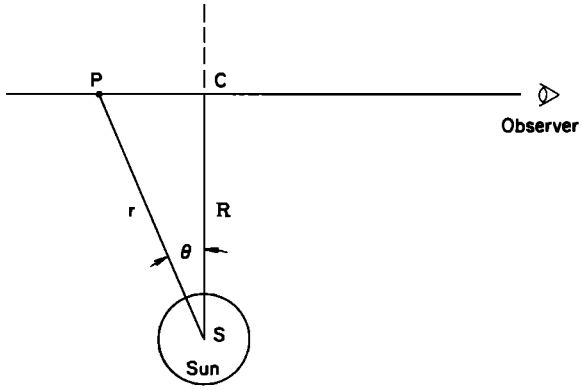

Fig. A1. The geometry used in describing scattering by coronal electrons. The plane of the drawing is defined by a line of sight through the corona and the center of the Sun S; C is the point along the line of sight that is closest to the Sun (at heliocentric distance R). *Billings* [1966] gives an expression for the light scattered by a "single scattering condensation" at a general point P along the line of sight, located at heliocentric distance r or a distance ℓ away from C. The value θ is the angular displacement of P from the "plane of the sky."

the total intensity (as with the SMM instrument) or the polarization brightness (as with the Mauna Loa instrument) of the scattered radiation. We will use these results to estimate the effects of "projection" of features distant from the limb on our statistical description of mass ejection and streamer latitudes and the comparison of those latitudes with the locations of other forms of solar activity.

Figure A1 is a sketch of the geometry useful in analyzing the scattering of photospheric radiation by coronal electrons. The plane of the drawing contains the center of the Sun S and a line of sight from an observer through the corona. The "plane of the sky," onto which all coronal features appear to be projected, is at right angles to the plane of the drawing, intersecting it along the line SC connecting the center of the Sun S with the point C where the line of sight is closest to the Sun. If the distance from S to C is denoted by R, a two-dimensional image of the coronal intensity $I(R, \Phi)$ can be constructed from observations made at different values of R and different angles Φ around the Sun (in different planes than that of the drawing).

The photospheric radiation incident at some point P along the line of sight has an oscillating electric (and magnetic) field that drives an oscillatory motion of any electrons at this location; the scattered light is radiated from these accelerated electrons. Since the intensity of the scattered radiation is anisotropic (as in dipole radiation from an oscillating current), its analysis requires determination of the components of the incident radiation (and the resulting electron motion) perpendicular to the line of sight. This basically geometric problem was solved by *Minneart* [1930], applied to the coronal scattering problem by *Van de Hulst* [1950], and summarized by *Billings* [1966, chap. 6, part B]. *Billings* [1966], p. 150] gives expressions for the light scattered along the line of sight by a "single-scattering condensation in the corona." Integration of all contributions along the line of sight yields the intensities of the two components of light that would be seen by the distant observer in Figure 14. The intensity (in units of energy per unit area, time, and solid angle) of the radiation polarized tangential to the solar limb (out of the plane of Figure 14) is

$$I_t = \frac{\pi\sigma}{2}\mathcal{T}_0 \int_{-\infty}^{\infty} n[(1-u)C + uD]\, dl$$

The intensity of the radiation polarized radial to the Sun is

$$I_r = \frac{\pi\sigma}{2}\mathcal{T}_0 \int_{-\infty}^{\infty} n[(1-u)(C - A\cos^2\theta) + u(D - B\cos^2\theta)]\, dl$$

In these expressions, l is the distance along the line of sight, measured from the point C in Figure 14, and θ is the angle out of the plane of the sky. The electron density is given by n, the constant σ is the Thomson cross section for scattering by electrons, and $\mathcal{T}_0$ is the intensity of photospheric radiation in the vertical (or radial) direction. The photospheric radiation has been taken to vary with direction as

$$I = \mathcal{T}_0(1 - u + u\cos^2\zeta)$$

where ζ is the angle between any ray of light and the direction radial to the Sun and the parameter u describes the degree of limb darkening of the radiation leaving the photosphere. If $u = 0$ the photospheric intensity is independent of ζ, while if $u = 1$ the photosphere intensity falls to zero as it is viewed at grazing incidence ($\zeta = \pi/2$). The quantities, A, B, C, and D are functions of the half angle Ω subtended by the Sun, viewed from a heliocentric direction r:

$$A = \cos\Omega \sin^2\Omega$$

$$B = -\frac{1}{8}\left[1 - 3\sin^2\Omega - \frac{\cos^2\Omega}{\sin\Omega} \cdot (1 + 3\sin^2\Omega)\ln\frac{1+\sin\Omega}{\cos\Omega}\right]$$

$$C = \frac{4}{3} - \cos\Omega - \frac{\cos^3\Omega}{3}$$

$$D = \frac{1}{8}\left[5 + \sin^2\Omega - \frac{\cos^2\Omega}{\sin\Omega}(5 - \sin^2\Omega)\ln\frac{1+\sin\Omega}{\cos\Omega}\right]$$

and where $\sin\Omega = R_0/r$ (with R_0 the solar radius).

The coronal observations dealt with in this paper involve two different combinations of the components I_t and I_r. The SMM observations of coronal mass ejections were in terms of the total intensity $I = I_t + I_r$ of scattered radiation; from above

$$I = \frac{\pi\sigma}{2}\mathcal{T}_0 \int_{-\infty}^{\infty} n[(1-u)(2C - A\cos^2\theta) + u(2D - B\cos^2\theta)]\, dl.$$

The Mauna Loa locations of bright coronal features were determined from scans of the "polarization brightness," pB at $R \approx 1.35R_0$; this quantity is defined as the difference of the components of the scattered radiation polarization in the

tangential and radial directions, in units of the photospheric intensity $\mathcal{T}_0$, or as $pB = (I_t - I_r)/\mathcal{T}_0$; again from above,

$$pB = \frac{\pi\sigma}{2}\int_{-\infty}^{\infty} n[(1-u)A + uB]\cos^2\theta\, dl.$$

Discussion and evaluation of these integrals is facilitated by writing the spatial variables r and l in terms of the angular displacement θ from the plane of the sky and changing the variable of integration to θ (integrating over the finite range $-\pi/2$ to $+\pi/2$). From Figure 14

$$r = \frac{R}{\cos\theta}$$

$$l = R\tan\theta$$

Then

$$dl = \frac{R}{\cos^2\theta}\, d\theta$$

$$I = \frac{\pi\sigma\mathcal{T}_0 R}{2}\int_{-\pi/2}^{\pi/2} n[(1-u)(2C - A\cos^2\theta) + u(2D - B\cos^2\theta)]\frac{d\theta}{\cos^2\theta}$$

$$pB = \frac{\pi\sigma R}{2}\int_{-\pi/2}^{\pi/2} n[(1-u)A + uB]\, d\theta$$

Our quantification of the visibility of coronal features will be based on these expressions.

The integrands in these expressions are sufficiently complicated that it is sometimes useful to simplify them by introducing a "point-source approximation" for the radiation from the photosphere. This approximation can be derived from simple geometric considerations by assuming that the light incident on electrons at point P of Figure 14 is polarized in the plane normal to a line connecting the Sun to P (or to SP on the figure). It can also be derived from taking the limiting forms of the integrands in the "finite source" expressions above as $\sin\Omega = R_0/r \to 0$. In this limit,

$$\frac{1}{\sin\Omega}\ln\frac{1+\sin\Omega}{\cos\Omega} \to 1 + \frac{1}{3}\sin^2\Omega$$

so that

$$A \to \sin^2\Omega = \left(\frac{R_0}{r}\right)^2$$

$$B \to \frac{2}{3}\sin^2\Omega = \frac{2}{3}\left(\frac{R_0}{r}\right)^2$$

$$C \to \sin^2\Omega = \left(\frac{R_0}{r}\right)^2$$

$$D \to \frac{2}{3}\sin^2\Omega = \frac{2}{3}\left(\frac{R_0}{r}\right)^2$$

The expressions for I and pB then take the forms

$$I \approx \frac{\pi\sigma}{2}\mathcal{T}_0\left(1 - \frac{u}{3}\right)R_0^2 R\int_{-\pi/2}^{\pi/2}\frac{n}{r^2}\frac{1+\sin^2\theta}{\cos^2\theta}\, d\theta$$

$$I = \frac{\pi\sigma}{2}\mathcal{T}_0\left(1 - \frac{u}{3}\right)\frac{R_0^2}{R}\int_{-\pi/2}^{\pi/2} n(1+\sin^2\theta)\, d\theta$$

$$pB \approx \frac{\pi\sigma}{2}\left(1 - \frac{u}{3}\right)R_0^2 R\int_{-\pi/2}^{\pi/2}\frac{n}{r^2}\, d\theta$$

$$pB = \frac{\pi\sigma}{2}\left(1 - \frac{u}{3}\right)\frac{R_0^2}{R}\int_{-\pi/2}^{\pi/2} n\cos^2\theta\, d\theta$$

The factor $1 - (u/3)$ relates the flux of radiation from the Sun to the intensity $\mathcal{T}_0$ for the limb-darkening law assumed above.

Intensity and Polarization Brightness in a Corona With a Spherically Symmetric, Power Law Density Distribution

A first step in examining the visibility of coronal features is the introduction of a "background" corona. As a simple example, let the electron density in the background corona be spherically symmetric and a function of an inverse power of the heliocentric distance, or

$$n = n_0\left(\frac{R_0}{r}\right)^\alpha$$

where n_0 is the electron density at the solar radius R_0. It is again convenient to write

$$r = \frac{R}{\cos\theta}$$

so that

$$n = n_0\left(\frac{R_0}{R}\right)^\alpha \cos^\alpha\theta$$

Substitution into the integrals for I and pB then gives

$$I = \pi\sigma\mathcal{T}_0 n_0\frac{R_0^\alpha}{R^{\alpha-1}}\int_0^{\pi/2}[(1-u)(2C - A\cos^2\theta) + u(2D - B\cos^2\theta)]\cos^{\alpha-2}\theta\, d\theta$$

$$pB = \pi\sigma n_0\frac{R_0^\alpha}{R^{\alpha-1}}\int_0^{\pi/2}[(1-u)A + uB]\cos^\alpha\theta\, d\theta$$

or in the point source approximation

$$I_{ps} = \pi\sigma\mathcal{T}_0 n_0\frac{R_0^{\alpha+2}}{R^{\alpha+1}}\int_0^{\pi/2}(1+\sin^2\theta)\cos^\alpha\theta\, d\theta$$

$$pB_{ps} = \pi\sigma n_0\frac{R_0^{\alpha+2}}{R^{\alpha+1}}\int_0^{\pi/2}\cos^{\alpha+2}\theta\, d\theta$$

Both of the latter expressions have the form of a constant times $R^{-(\alpha+1)}$. We defined R as the shortest heliocentric

distance to the line of sight (Figure 14); it is also, of course, the heliocentric distance at which the line of sight is "projected" onto the plane of the sky. In an image or a scan of the corona, this is the heliocentric distance one would assign to a measurement of the light scattered along the line of sight. Observation of a spherically symmetric background corona, with an electron density that falls as a power of the heliocentric distance r, would reveal scattered radiation that did not depend on angle around the Sun but with an intensity or polarization brightness that fell off one power of R more steeply than the density. This effect stems from the r^{-2} factor in the radiation from a point source and the integration along the line of sight, which introduces a single positive power of r. No such simple characterization of the radial dependence of I or pB can be given for the finite source expressions; the dependence on r is partly contained in the quantities, A, B, C, and D, which are complicated functions of $\sin \Omega = R_0/r$.

The integrals in the "point source" expressions for the quantities I and pB can be easily evaluated to give the approximations

$$I_{ps} = \pi\sigma\mathcal{T}_0 n_0 \frac{R_0^{\alpha+2}}{R^{\alpha+1}} \frac{\alpha+3}{\alpha+2} \int_0^{\pi/2} \cos^\alpha \theta \, d\theta$$

$$I_{ps} = \frac{\pi\sigma\mathcal{T}_0 R_0^{\alpha+2} n_0}{2R^{\alpha+1}} \frac{\alpha+3}{\alpha+2} \cdot \frac{\alpha-1}{\alpha} \cdot \frac{\alpha-3}{\alpha-2} \cdot \cdots \frac{3}{4} \cdot \frac{\pi}{2}$$

for α even

$$I_{ps} = \frac{\pi\sigma\mathcal{T}_0 R_0^{\alpha+2}}{R^{\alpha+1}} \frac{\alpha+3}{\alpha+2} \cdot \frac{\alpha-1}{\alpha} \cdot \frac{\alpha-3}{\alpha-2} \cdot \cdots \frac{2}{3}$$

for α odd

$$pB_{ps} = \pi\sigma n_0 \frac{R_0^{\alpha+2}}{R^{\alpha+1}} \frac{\alpha+1}{\alpha+2} \int_0^{\pi/2} \cos^\alpha \theta \, d\theta$$

$$pB_{ps} = \frac{\pi\sigma R_0^{\alpha+2} n_0}{2R^{\alpha+1}} \frac{\alpha+1}{\alpha+2} \cdot \frac{\alpha-1}{\alpha} \cdot \frac{\alpha-3}{\alpha-2} \cdot \cdots \frac{3}{4} \cdot \frac{\pi}{2}$$

for α even

$$pB_{ps} = \frac{\pi\sigma R_0^{\alpha+2}}{R^{\alpha+1}} \frac{\alpha+1}{\alpha+2} \cdot \frac{\alpha-1}{\alpha} \cdot \frac{\alpha-3}{\alpha-2} \cdot \cdots \frac{2}{3}$$

for α odd

These expressions also imply that the polarization,

$$p = \frac{I_t - I_r}{I_t + I_r} = \frac{pB \times \mathcal{T}_0}{I}$$

has the constant value (independent of heliocentric distance)

$$p_{ps} = \frac{\alpha+1}{\alpha+3}$$

These point source expressions for I_{ps}, pB_{ps}, and p_{ps} should be understood as approximations that become increasingly valid at large heliocentric distances, or for $R \gg R_0$.

Coronal observations made during solar eclipses have traditionally been used to deduce models of the variation in an average coronal density with height or heliocentric distance [e.g., *Billings*, 1966; *Newkirk*, 1967; *Allen*, 1973]. The $n(r)$ derived in this manner are appropriate functions for use as a background corona in this discussion. However, they can be described by a simple power law only within limited ranges of heliocentric distance; sums of several inverse powers of r are needed to describe the functions over a wide range of r.

Most of the SMM observations of coronal mass ejections were made at apparent heliocentric distances R between 2 and 3 solar radii. The coronal electron densities tabulated by *Allen* [1973] in this range of heliocentric distance vary approximately as r^{-5}. We will thus use

$$n = n_0 \left(\frac{R_0}{r}\right)^5$$

as a background corona in this discussion (or $\alpha = 5$ in the expressions derived above). The actual values of $n(r)$ deduced from eclipse observations fall more rapidly than r^{-5} at smaller r, more slowly than r^{-5} at larger r. This difference must be borne in mind when applying any results of this discussion to observations made at different heliocentric distances.

For $\alpha = 5$, the integrals giving the total intensity and polarization brightness of the scattered light are

$$I = \pi\sigma\mathcal{T}_0 n_0 R_0 \left(\frac{R_0}{R}\right)^4 \int_0^{\pi/2} [(1-u)(2C - A\cos^2\theta) + u(2D - B\cos^2\theta)] \cos^3\theta \, d\theta$$

$$pB = \pi\sigma n_0 R_0 \left(\frac{R_0}{R}\right)^4 \int_0^{\pi/2} [(1-u)A + uB] \cos^5\theta \, d\theta$$

In the point source approximation these integrals become

$$I \approx \pi\sigma\mathcal{T}_0 n_0 R_0 \left(\frac{R_0}{R}\right)^6 \int_0^{\pi/2} (1 + \sin^2\theta) \cos^5\theta \, d\theta$$

$$pB \approx \pi\sigma n_0 R_0 \left(\frac{R_0}{R}\right)^6 \int_0^{\pi/2} \cos^7\theta \, d\theta$$

The integrands in these expressions are plotted on Figures A2 and A3 for different values of the heliocentric distance R. Figure 15 shows the scattering functions

$$i(\theta) = \frac{(R/R_0)^2}{1 - u/3} [(1-u)(2C - A\cos^2\theta) + u(2D - B\cos^2\theta)] \cos^3\theta$$

or the integrand in the "finite source" expression for total intensity, normalized by the factors $(1 - u/3)^{-1}$ to the radiative flux from the Sun and $(R/R_0)^2$ to make the R^{-6} dependence for large R explicit (and facilitate comparison with the point source approximation). The solid curves show $i(\theta)$ for three values for the limb-darkening parameter u:

No limb darkening

$$u = 0,$$

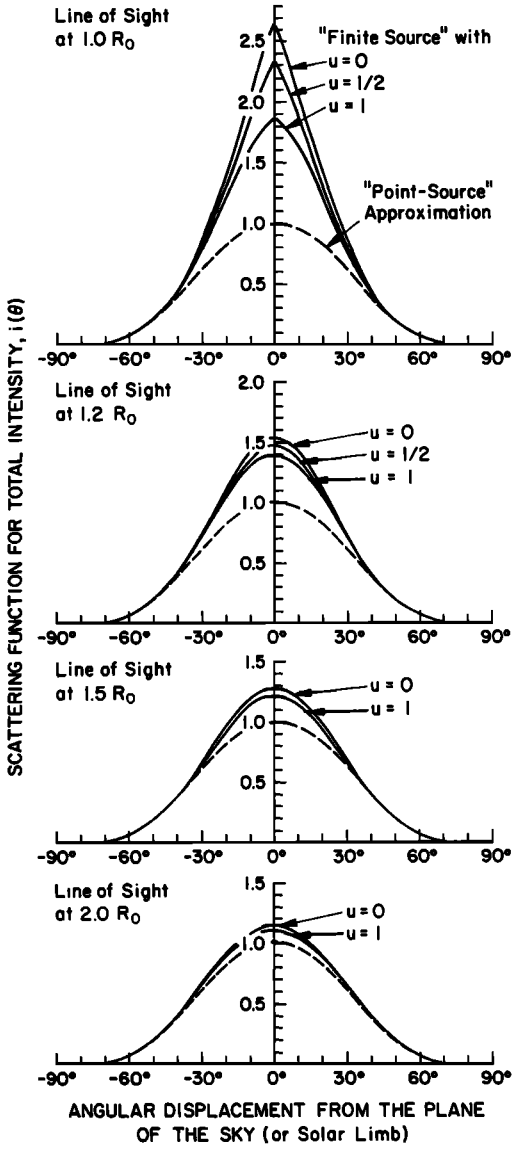

Fig. A2. The functions $i(\theta)$ for scattering of radiation along lines of sight passing through a spherically symmetric background corona, with $n \propto r^{-5}$, at heliocentric distances R; the area under each curve is proportional to the total intensity of light seen at R. The four panels show $i(\theta)$ at R = 1.0, 1.2, 1.5, and 2 solar radii (R_0). The solid lines represent the scattering for a finite-sized Sun with different degrees of limb darkening of photospheric radiation: u = 0, no limb darkening; u = 1, extreme limb darkening; and u = 1/2 (at R = 1 and 1.2 R_0 only), intermediate limb darkening. The dashed lines give the scattering function $i_{ps}(\theta)$ for a point source Sun. The effects of limb darkening and the error in the point source approximation diminish with increasing R.

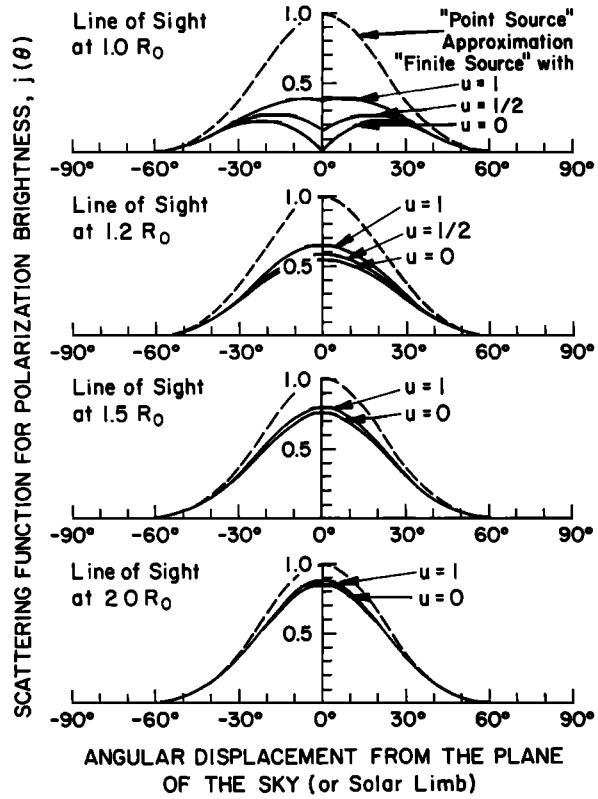

Fig. A3. The functions $j(\theta)$ for scattering of radiation along lines of sight passing through a spherically symmetric background corona, with $n \propto r^{-5}$, at heliocentric distances R; the area under each curve is proportional to the polarization brightness seen at R. The four panels show $j(\theta)$ at R = 1.0, 1.2, 1.5, and 2 solar radii (R_0). The solid lines represent the scattering for a finite-size Sun with different degrees of limb darkening of photospheric radiation: u = 0, no limb darkening; u = 1, extreme limb darkening, and u = 1/2 (at R = 1 and 1.2 R_0 only), intermediate limb darkening. The dashed lines give the scattering function $j_{ps}(\theta)$ for a point source Sun. The effects of limb darkening and the error in the point source approximation are large near $R = R_0$ but diminish with increasing R.

Extreme limb darkening

$$u = 1,$$

Intermediate limb darkening

$$u = 1/2,$$

and for four values of R; R = 1.0, 1.2, 1.5, and 2 R_0. The dashed curves on Figure 15 shows the scattering function

$$i_{ps}(\theta) = \frac{(1 + \sin^2\theta)\cos^5\theta}{1 - u/3}$$

or the integrand in the point source expression for total intensity, again normalized in terms of the radiative flux from the photosphere. For $R = R_0$, or a line of sight that passes through the base of the corona, the finite source scattering functions are sharply peaked near $\theta = 0$ or the plane of the sky; they are substantially larger than the point source scattering function for all values of the parameter u. As would be expected, the point source approximation is very poor close to the Sun; it seriously underestimates the scattering near the plane of the sky because of the assumption that all photospheric radiation is polarized in a plane normal to the radial direction. As R increases (through the values 1.2, 1.5, and 2 R_0 on the figure) the finite source scattering functions become smoother and broader, approaching the point source function (from above) as the Sun subtends smaller angles when viewed from larger heliocentric distances. The differences between the functions for different values of u also diminish as R increases (only the u = 0 and u = 1 functions are shown for R = 1.5 and 2 R_0);

as the photospheric radiation is confined within a diminishing angle the distribution of intensity within that angle has little effect on the polarization of the radiation incident on the scatterers. Within the nominal 2 to 3 R_0 range of heliocentric distance spanned by the SMM observations, the point source scattering function is always within 15% of the finite source functions.

Figure A3 shows the similarly normalized scattering functions

$$j(\theta) = \frac{(R/R_0)^2}{1 - u/3}\,[(1 - u)A + uB]\cos^5\theta$$

or the integrand in the finite source expression for the polarization brightness. The solid lines show $j(\theta)$ for the same three values of the limb-darkening parameter and the same values of the heliocentric distance as above. The dashed curves on Figure 16 shows the normalized scattering function

$$j_{ps}(\theta) = \frac{\cos^7\theta}{1 - u/3}$$

or the integrand in the point source expression for the polarization brightness. For $R = R_0$ the finite source scattering functions are always smaller than the point source functions and are significantly depressed near $\theta = 0$ (or the plane of the sky). This depression arises from the presence of photospheric light incident on scattering electrons from directions well away from the radial; this leads to a significant component of the scattered light, I_r, in the radial direction and thus a reduction in the difference $I_t - I_r$ that defines the polarization brightness. The effect is, of course, most pronounced when there is no limb darkening ($u = 0$) and diminished when limb darkening is present ($u = 1/2$ and 1). As R increases (through the values 1.2, 1.5, and 2.0 R_0 on the figure), the central depression in the finite-source scattering functions disappears; the functions become smoother and narrower; approaching the point source function (from below) as the Sun subtends smaller angles when viewed from larger heliocentric distances. The differences between the functions for different values of u again diminish as R increases (only the $u = 0$ and $u = 1$ functions are shown for $R = 1.5$ and 2 R_0).

The point source approximations to the integrals for I and pB with $\alpha = 5$ are

$$I_{ps} = \frac{64}{105}\,\pi\sigma\mathcal{T}_0 n_0 R_0\left(\frac{R_0}{R}\right)^6$$

$$pB_{ps} = \frac{16}{35}\,\pi\sigma n_0 R_0\left(\frac{R_0}{R}\right)^6$$

Surprisingly (at least to the author), the finite Sun expressions for I and pB with $\alpha = 5$ and $u = 0$, or no limb darkening

$$I = \pi\sigma\mathcal{T}_0 n_0 R_0\left(\frac{R_0}{R}\right)^4 \int_0^{\pi/2} (2C - A\cos^2\theta)\cos^3\theta\,d\theta$$

$$I = \pi\sigma\mathcal{T}_0 n_0 R_0\left(\frac{R_0}{R}\right)^4 \int_0^{\pi/2} \left(\frac{8}{3} - 2\cos\Omega - \frac{2}{3}\cos^3\Omega - \cos\Omega\sin^2\Omega\cos^2\theta\right)\cos^3\theta\,d\theta$$

(where $\sin\Omega = R_0/R\cos\theta$) and

$$pB = \pi\sigma n_0 R_0\left(\frac{R_0}{R}\right)^4 \int_0^{\pi/2} A\cos^5\theta\,d\theta$$

$$pB = \pi\sigma n_0 R_0\left(\frac{R_0}{R}\right)^4 \int_0^{\pi/2} \cos\Omega\sin^2\Omega\cos^5\theta\,d\theta$$

can be evaluated analytically to give

$$\begin{aligned} I = \pi\sigma\mathcal{T}_0 n_0 R_0\left(\frac{R_0}{R}\right)^4 \Bigg\{ & \frac{16}{9} - \frac{1}{4}\left(\frac{R}{R_0}\right)^2\Bigg[3\left(\frac{R_0}{R}\right)^2 - 1 \\ & + \frac{1}{2}\left(\frac{R}{R_0} + 2\frac{R_0}{R} - 3\frac{R_0^3}{R^3}\right)\ln\frac{1 + R_0/R}{1 - R_0/R}\Bigg] \\ & - \frac{1}{72}\left(\frac{R}{R_0}\right)^2\Bigg[-3 + 22\left(\frac{R_0}{R}\right)^2 - 15\left(\frac{R}{R_0}\right)^4 \\ & + \frac{3}{2}\left(\frac{R}{R_0}\right)\left(1 - \frac{R_0^2}{R^2}\right)^2\left(1 + 5\frac{R_0^2}{R^2}\right)\ln\frac{1 + R_0/R}{1 - R_0/R}\Bigg] \\ & - \frac{1}{48}\left(\frac{R}{R_0}\right)^2\Bigg[15\left(\frac{R_0}{R}\right)^4 + 6\left(\frac{R_0}{R}\right)^2 - 9 \\ & + \frac{3}{2}\left(\frac{R}{R_0}\right)\left(1 - \frac{R_0^2}{R^2}\right)\left(3 + 5\frac{R_0^2}{R^2}\right)\ln\frac{1 + R_0/R}{1 - R_0/R}\Bigg] \\ & + \frac{1}{48}\left(\frac{R}{R_0}\right)^5\Bigg[6\left(\frac{R_0}{R}\right)^7 + \left(\frac{R_0}{R}\right)^5\left(1 - \frac{R_0^2}{R^2}\right) \\ & - \frac{5}{8}\left(\frac{R_0}{R}\right)\left(1 - \frac{R_0^2}{R^2}\right)^2\left(5\frac{R_0^2}{R^2} - 3\right) \\ & - \frac{15}{16}\left(1 - \frac{R_0^2}{R^2}\right)^4\ln\frac{1 + R_0/R}{1 - R_0/R}\Bigg]\Bigg\} \end{aligned}$$

$$\begin{aligned} pB = \frac{1}{48}\,\pi\sigma n_0 R_0\left(\frac{R_0}{R}\right)^2 \Bigg\{ & 15\left(\frac{R_0}{R}\right)^4 + 6\left(\frac{R_0}{R}\right)^2 - 9 \\ & + \frac{3}{2}\left(\frac{R}{R_0}\right)\left(1 - \frac{R_0^2}{R^2}\right)\left(3 + 5\frac{R_0^4}{R}\right)\ln\frac{1 + R_0/R}{1 - R_0/R} \\ & - \left(\frac{R}{R_0}\right)^3\Bigg[6\left(\frac{R_0}{R}\right)^7 + \left(\frac{R_0}{R}\right)^5\left(1 - \frac{R_0^2}{R^2}\right) \\ & - \frac{5}{8}\left(\frac{R_0}{R}\right)\left(1 - \frac{R_0^2}{R^2}\right)^2\left(5\frac{R_0^2}{R^2} - 3\right) \\ & - \frac{15}{16}\left(1 - \frac{R_0^2}{R^2}\right)^4\ln\frac{1 + R_0/R}{1 - R_0/R}\Bigg]\Bigg\} \end{aligned}$$

These expressions illustrate dramatically the advantage of using the simple point source expression whenever possible; they can also provide a fascinating experience for the reader

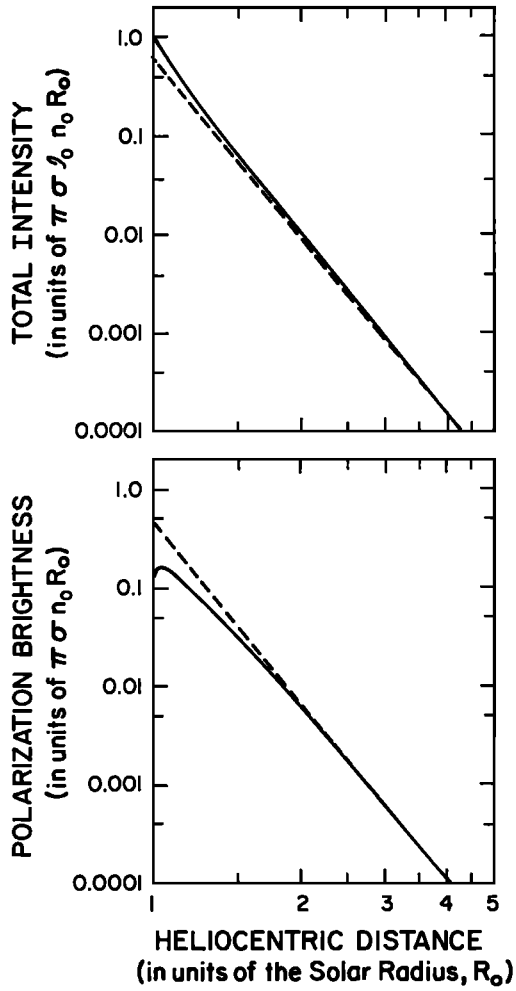

Fig. A4. The radial variations in the total intensity and polarization brightness of the radiation scattered by the $n \propto r^{-5}$ background corona along lines of sight with R in the range 1 R_0 to 4.3 R_0. The solid curves show the variations for a finite Sun with no limb darkening; the dashed curves show the variations in the point source approximation. The increasing validity of the point source approximation as R increases is evident. The total intensity and polarization brightness variations for the finite Sun with values of the limb-darkening parameter u between 0 and 1 fall between the two curves shown on this figure.

who wishes to show that they do approach the point source approximations as $R \rightarrow \infty$.

Figure A4 shows the radial variations in I and pB given by the finite source expressions with no limb-darkening (solid curves) and the point source expression (dashed curves). Looking first at the intensity functions, the finite source $I(R)$ is always larger than the point source approximation $I_{ps}(R)$. Further, since the intensity I is the area under the appropriate scattering function curve as shown on Figure A2, the intensities for other values of the limb-darkening parameter u in the range 0 to 1 will fall between the $I(R)$ and $I_{ps}(R)$ curves on Figure A4. The ratio I_{ps}/I at several values of R is given in Table A1. The point source expression seriously underestimates the intensity of scattered light for R near R_0 but, as expected, becomes a better estimate as R increases; the percentage error in the point source expression relative to the finite Sun expression for no limb darkening is 45% near $R = R_0$ but drops to 10% at $R = 2\ R_0$ or 4% at $R = 3$

TABLE A1. A Comparison of the Point Source and Finite Sun (no Limb Darkening) Expressions for Intensity I and Polarization Brightness pB

R/R_0	I_{ps}/I	pB_{ps}/pB
1.0	0.5555	3.657
1.1	···	1.958
1.2	0.7454	1.633
1.5	0.8452	1.2871
2.0	0.9026	1.1342
3.0	0.9627	1.0534

R_0. For other, more realistic values of the limb darkening parameter, the errors in the point source approximation are smaller than those given in Table A1.

In contrast, the finite source $pB(R)$ is always smaller than the point source approximation $pB_{ps}(R)$. Again, the polarization brightness for other values of the limb-darkening parameter u between 0 and 1 will fall between the $pB(R)$ and $pB_{ps}(R)$ curves on Figure A4. The ratio pB_{ps}/pB is given in Table A1 for several values of R. The point source approximation seriously overestimates the polarization brightness for R near R_0 but rapidly becomes a better estimate as R increases; the percentage error relative to the finite Sun (no limb-darkening) expression as 200% at $R = R_0$ but drops rapidly to 13% at $R = 2\ R_0$ or 5% at 3 R_0.

The goal of this lengthy analysis is to understand the visibility of coronal features that are not over the solar limb (or near the plane of the sky). The first hints at this understanding are contained in the shapes of the scattering functions in Figure A2 and A3 for the spherically symmetric, $n \propto r^{-5}$ background atmosphere used in this discussion. For the total intensity, the finite Sun scattering functions $i(\theta)$ at $R = R_0$ decrease with displacement from the plane of the sky ($\theta = 0$) to half of their $\theta = 0$ value at $\theta = 22°$ for $u = 0$ (no limb darkening) or $\theta = 26°$ for $u = 1$ (extreme limb darkening). As R increases, these half widths at half maximum amplitude increase slowly, approaching the value of 34.6° that pertains to the point-source approximation as R becomes large. For example, these half angles at $R = 2\ R_0$ are close to 33° for $u = 0$ or $u = 1$. For the polarization brightness, the finite Sun scattering functions $j(\theta)$ at $R = R_0$ are flattened or even depressed near the plane of the sky but decrease with displacements from that plane greater than ~20°. These functions fall to half of their maximum values (not attained at $\theta = 0$) for $\theta = 39°$ ($u = 0$), 37° ($u = 1/2$) and 33° ($u = 0$). For $R = 1.2\ R_0$ the flattening near $\theta = 0$ has disappeared and the functions fall to half of their maximum values (attained at $\theta = 0$) for θ near 28° for all u in the range 0 to 1. As R increases still further, the half widths rapidly approach the 25.1° value that pertains to the point source approximation.

We can thus conclude that most of the contributions to the total intensity of scattered light come from within 35° of the plane of the sky. Except at heliocentric distances close to R_0, most of the contributions to the polarization brightness of scattered light come from a slightly smaller range of angle near the plane of the sky, with the half width approaching 25° for large R.

These conclusions can be sharpened in the point source approximation by direct determination of the fraction of the total intensity or polarization brightness attained when the

scattering functions are integrated over a range $\pm\Theta$ rather than $\pm\pi/2$. Again, for our standard "background" corona with $\alpha = 5$, 82% of the total intensity is produced by the scattering within the $\pm 35°$ half width of the point source scattering function; half of the actual intensity of scattered light comes from within $\pm 18°$ of the plane of the sky. For the same model, 77% of the polarization brightness is produced by scattering within the 25° half width of the point source scattering function; half of the actual polarization brightness comes from within $\pm 13°$ of the plane of the sky.

Visibility of Bright Features Immersed in a Background Corona

The visibility of a bright feature immersed in a background corona with a spherically symmetric, power law density distribution of electron density is also analyzed easily under a reasonable simplifying assumption; the enhanced density in the feature (along the line of sight) will be assumed to be a multiple of the background density over some range of the angle θ. If the background density is written as

$$n_b(r) = n_{b0}\left(\frac{R_0}{r}\right)^5 = n_{b0}\left(\frac{R_0}{R}\right)^5 \cos^5\theta$$

and the density in the feature as

$$n(r) = \eta n_b(r) \qquad \theta_1 < \theta < \theta_2$$

the integral for the observed intensity is

$$I = \frac{\pi\sigma\mathcal{J}_0 n_{b0}R_0}{2}\left(\frac{R_0}{R}\right)^4\left\{\int_{-\pi/2}^{\theta_1}[(1-u)(2C - A\cos^2\theta) + u(2D - B\cos^2\theta)]\cos^3\theta\, d\theta + \eta\int_{\theta_1}^{\theta_2}[(1-u)(2C - A\cos^2\theta) + u(2D - B\cos^2\theta)]\cos^3\theta\, d\theta + \int_{\theta_2}^{\pi/2}[(1-u)(2C - A\cos^2\theta) + n(2D - B\cos^2\theta)]\cos^3\theta\, d\theta\right\}$$

$$I = \frac{\pi\sigma\mathcal{J}_0 n_{b0}R_0}{2}\left(\frac{R_0}{R}\right)^4\left\{\int_{-\pi/2}^{\pi/2}[(1-u)(2C - A\cos^2\theta) + u(2D - B\cos^2\theta)]\cos^3\theta\, d\theta + (\eta-1)\int_{\theta_1}^{\theta_2}[(1-u)\cdot(2C - A\cos^2\theta) + u(2D - B\cos^2\theta)]\cos^3\theta\, d\theta\right\}$$

The first integral in the last expression is precisely the intensity of scattered light in the background coronal introduced above; denoting this as I_b where

$$I_b = \pi\sigma\mathcal{J}_0 n_{b0}R_0\left(\frac{R_0}{R}\right)^4\int_{-\pi/2}^{\pi/2}[(1-u)(2C - A\cos^2\theta) + u(2D - B\cos^2\theta)]\cos^3\theta\, d\theta$$

we have

$$I = I_b + (\eta-1)\frac{\pi\sigma\mathcal{J}_0 n_{b0}R_0}{2}\left(\frac{R_0}{R}\right)^4\int_{\theta_1}^{\theta_2}[(1-u)(2C - A\cos^2\theta) + u(2D - B\cos^2\theta)]\cos^3\theta\, d\theta$$

The visual contrast of the bright feature can be defined as the excess over background, normalized to that same background intensity, or as

$$K_I = \frac{I - I_b}{I_b}$$

Then

$$K_I = (\eta-1)\frac{\pi\sigma\mathcal{J}_0 n_{b0}R_0}{2I_b}\left(\frac{R_0}{R}\right)^4\int_{\theta_1}^{\theta_2}[(1-u)(2C - A\cos^2\theta) + u(2D - B\cos^2\theta)]\cos^3\theta\, d\theta$$

For a given background density $n_b(r)$ and excess density parameter $\eta - 1$, this contrast can be regarded as a function of the central location

$$\bar{\theta} = \frac{\theta_1 + \theta_2}{2}$$

of the density enhancement.

An entirely parallel development leads to an expression for the visual contrast of the feature in the polarization brightness of the scattered light

$$K_{pb}(\bar{\theta}) = (\eta-1)\frac{\pi\sigma n_{b0}R_0}{2pB_b}\left(\frac{R_0}{R}\right)^4\int_{\theta_1}^{\theta_2}[(1-u)A + uB]\cos^5\theta\, d\theta$$

where the background polarization brightness pB_b is

$$pB_b = \pi\sigma n_{b0}R_0\left(\frac{R_0}{R}\right)^4\int_0^{\pi/2}[(1-u)A + uB]\cos^5\theta\, d\theta$$

Case 1: A narrow density enhancement. The utility of these manipulations is most obvious if the density enhancement is confined to a narrow range of angles, or $\theta_2 - \theta_1$ is small. Then

$$K_I(\bar{\theta}) \approx (\eta-1)\frac{\pi\sigma\mathcal{J}_0 R_0}{2I_b}\left(\frac{R_0}{R}\right)^4 n_{b0}(\theta_2 - \theta_1)[(1-u)(2C - A\cos^2\bar{\theta} + u(2D - B\cos^2\bar{\theta})]\cos^3\bar{\theta}$$

where the functions A, B, C, and D are evaluated at $\bar{\theta}$. Writing

$$N = (\eta-1)(\theta_2 - \theta_1)n_{b0}R_0$$

as the number of excess electrons in the coronal feature (per unit area along the line of sight) and using

$$i(\theta) = \frac{(R/R_0)^2}{1 - u/3}[(1-u)(2C - A\cos^2\theta) + u(2D - B\cos^2\theta)]\cos^3\theta$$

as defined above and plotted in Figure A2,

TABLE A2. Visibility of Coronal Features of Different Widths

Angular Distance From the Limb	Narrow	Relative Contrast					
		10°	20°	30°	40°	50°	60°
0°	1.000	1.000	1.000	1.000	1.000	1.000	1.000
5°	0.989	0.989	0.988	0.988	0.988	0.988	0.989
10	0.954	0.954	0.954	0.954	0.953	0.954	0.956
15	0.897	0.987	0.896	0.896	0.896	0.899	0.903
20	0.818	0.818	0.818	0.819	0.822	0.826	0.836
25	0.721	0.721	0.722	0.726	0.731	0.741	0.755
30	0.609	0.610	0.614	0.620	0.631	0.646	0.667
35	0.490	0.492	0.499	0.510	0.526	0.547	0.574
40	0.373	0.375	0.385	0.400	0.422	0.449	0.482
45	0.265	0.268	0.280	0.298	0.324	0.356	0.393
50	0.174	0.178	0.191	0.211	0.234	0.271	0.311
55	0.104	0.108	0.120	0.139	0.165	0.198	0.237
60	0.055	0.058	0.068	0.085	0.108	0.137	0.172
65	0.025	0.027	0.035	0.047	0.066	0.090	0.120
70	0.009	0.010	0.015	0.020	0.037	0.054	0.078
75	0.002	0.003	0.006	0.010	0.018	0.030	0.047
80	0.000	0.001	0.002	0.003	0.008	0.015	0.026
85	...	0.000	0.000	0.001	0.003	0.007	0.013
90	...	...	...	0.000	0.001	0.002	0.005

$$K_I(\bar{\theta}) \approx \frac{\pi\sigma\mathcal{F}_0}{2I_b}\left(\frac{R_0}{R}\right)^6 (1 - u/3)Ni(\bar{\theta})$$

What is of primary interest here is the variation in visual contrast as a function of angular displacement from the limb, or the dependence upon $\bar{\theta}$ of $K_I(\bar{\theta})$, when normalized to its value for a given feature seen at the limb or $\bar{\theta} = 0$. We thus define

$$\kappa_I(\bar{\theta}) = \frac{K_I(\bar{\theta})}{K_I(0)}.$$

For the approximation developed above this becomes

$$\kappa_I(\bar{\theta}) = i(\bar{\theta})$$

which is simply the scattering function of Figure A2. A parallel development for the polarization brightness leads to the expression for the angular variation in the visual contrast of a narrow feature seen in pB,

$$\kappa_{pB}(\bar{\theta}) = \frac{K_{pB}(\bar{\theta})}{K_{pB}(0)} = j(\theta)$$

where $j(\theta)$ is the scattering function for polarization brightness defined above and plotted in Figure A3.

These results are extremely simple. Whatever the visual contrast of a bright, narrow coronal feature when at the limb ($\bar{\theta} = 0$), that contrast will decline with angular displacement θ from the limb in the same manner as the scattering functions $i(\theta)$ and $j(\theta)$ plotted on Figure A2 and A3. It is also simple to generalize the results (for the case of the narrow density enhancement) to other distributions of density in the background corona. For the $n \propto r^{-5}$ background used here, the contrast in intensity will be cut in half for $\theta \approx 35°$ while the contrast in polarization brightness will be cut in half for $\theta \approx 25°$. The bright feature will become unidentifiable when its contrast is sufficiently low to be lost in the noise level of coronal images or scans. The angular displacement from the limb at which this occurs will be greater for bright features than for dim features. In a statistical analysis such as that in the text, we should estimate this displacement for a typical feature. From our experience with both SMM and Mauna Loa data, we suggest that the typical mass ejection or coronal ray has a contrast about a factor of two or less above the noise level in the background corona. Thus the half power point $\theta = 35°$ is a reasonable estimate for the range of visibility for narrow bright features seen in the SMM images that reveal the total intensity of the radiation scattered in the corona. For the Mauna Loa observations made in polarization brightness of the scattered radiation, the half power width of 25° is a rough estimate for the range of visibility. At the heliocentric distance of $\sim 1.35\ R_0$ where the Mauna Loa scans used in this paper were made, the half width at half power should be slightly wider than 25°. However, the density in the lower corona falls off more rapidly than r^{-5}, and this should sharpen the scattering functions near $\theta = 0$ and lead to a slightly smaller half width.

Case 2: A broad density enhancement. For broad density enhancements, similar normalized visual contrasts can be defined. Evaluation of the integrals in these expressions is relatively simple for the power law background corona, in the point source approximation. Table A2 records some of these results for our familiar $n \propto r^{-5}$ assumption. The seven columns pertain to a narrow enhancement as in case 1 and to enhancements that have total angular widths of 10°, 20°, 30°, 40°, 50°, and 60° (in the direction along the line of sight). The table indicates that the visibility of the finite width enhancements decreases with angular displacement from the Sun only slightly more slowly than the narrow enhancement. Thus the use of the 35° and 25° values for the limits of visibility in I and pB should remain reasonable estimates for all but the widest coronal mass features. The comparisons of the finite Sun and point source scattering functions in Figures A2 and A3 also suggest that this conclusion can be applied to the more realistic case of the finite Sun as long as the region of $R \lesssim 1.2\ R_0$ (where the scattering functions have significantly different shapes) is avoided.

APPENDIX B: PROJECTED LATITUDES OF FEATURES OFF THE SOLAR LIMB

Figure B1 is a sketch of the geometry pertinent to the projection of a coronal feature onto the plane of the sky. A straight, radial line extends outward from the surface of a sphere (such as the Sun), at a latitude (or angle to the "equatorial plane") λ and at a longitude (or rotation about the polar axis) displacement from the central meridian of ψ, as shown in the top panel. The view projected onto the plane of the sky for an observer in the solar equatorial plane is shown in the bottom panel; the radial line will appear at an angle Λ from the solar equator with $\Lambda > \lambda$ (unless $\psi = 90°$) because of the fore-shortening of the "y" coordinate of any point on the line. Working in units of the radius of the sphere, it is clear that

$$\sin \Lambda = \frac{z}{\sqrt{y^2 + z^2}}$$

$$\sin^2 \Lambda = \frac{\sin^2 \lambda}{\sin^2 \lambda + \cos^2 \lambda \sin^2 \psi}$$

$$\sin^2 \Lambda = \frac{1}{1 + \cot^2 \lambda \sin^2 \psi}$$

The angle β between this radial line and the x axis in Figure B2 is given by

$$\cos \beta = |x| = \cos \lambda \cos \psi$$

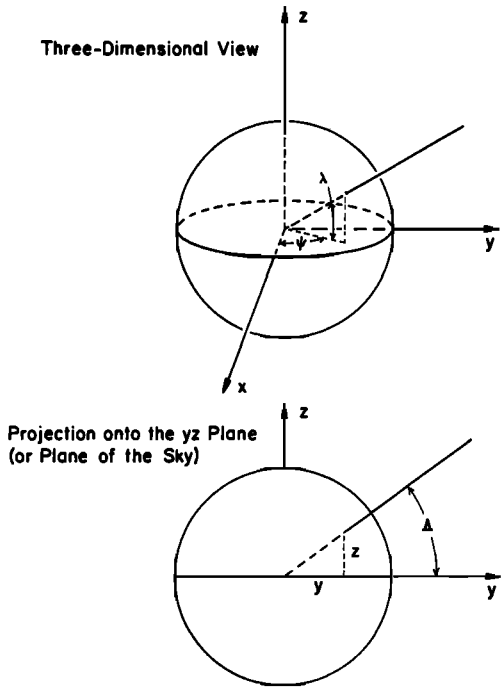

Fig. B1. The geometry useful in describing the projection of coronal features onto the plane of the sky. (Top) A radial line extending outward from the Sun at a latitude λ and a longitude ψ measured from the "central meridian" for an observer. The x axis points from the Sun to an equatorial observer, the z axis passes through the pole of the Sun, and the y axis is chosen to give an orthogonal coordinate system. (Bottom) The projection of the same radial line onto the yz plane, with projected latitude Λ.

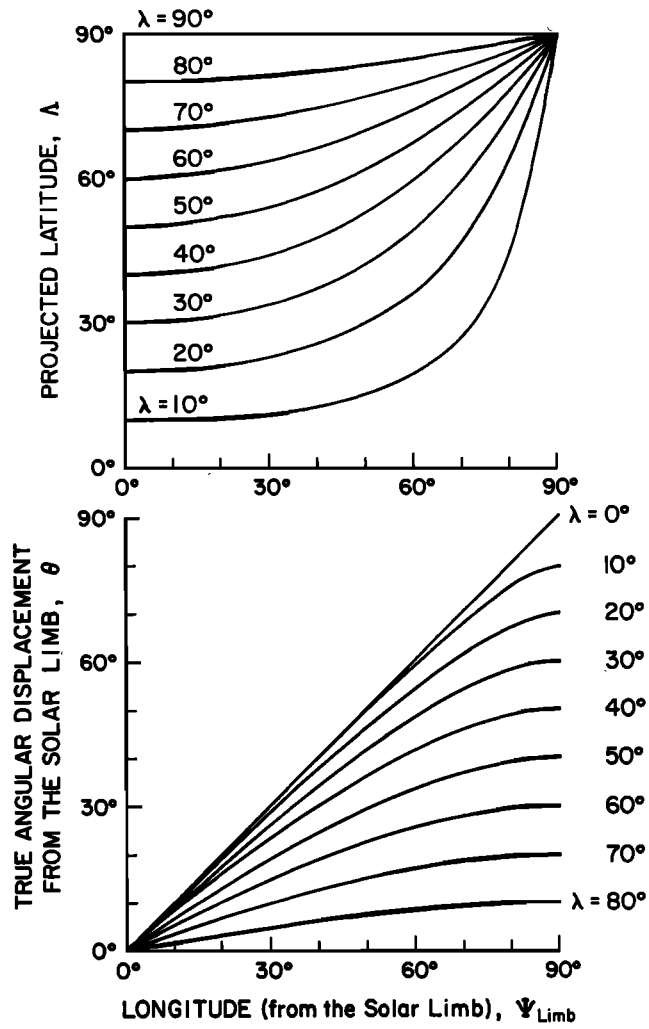

Fig. B2. A quantification of the projection effects. (Top) The projected latitude Λ for radial feature at true latitude λ and longitude ψ_{limb} away from the limb. (Bottom) The actual angular displacement of the feature from the yz plane (or plane of the sky).

This is the compliment of the angle θ between the line and the yz plane (i.e., the angular displacement from the plane of the sky or the solar limb), so that

$$\sin \theta = \cos \lambda \cos \psi$$

In exploring these relationships it is convenient to measure longitude from the solar limb, or as $\psi_{Limb} = 90 - \psi$. The top panel of Figure B2 is a plot of the projected latitude Λ as a function of ψ_{Limb} for values of the true latitude λ in 10° increments. The bottom panel of Figure B1 is a plot of the true angular displacement θ from the solar limb as a function of ψ_{Limb} for the same values of true latitude λ. Examination of the former reveals that a radial coronal feature can appear at any projected latitude $\Lambda > \lambda$; Λ increases with longitude measured from the limb until $\Lambda = 90°$ for all features at central meridian, (except for a singular equatorial feature with $\lambda = 0$). This increase is slow and rather uniform for features at high true latitudes but occurs largely at locations near central meridian for features at low true latitudes. Examination of the bottom panel reveals that the displacement θ from the limb increases nearly linearly with ψ_{Limb} for low-latitude features, approaching the colatitude $90° - \lambda$ at

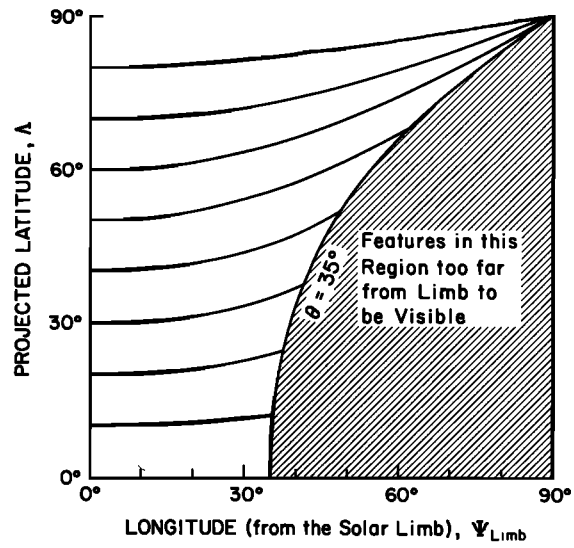

Fig. B3. Projected latitudes for radial features within 35° of the plane of the sky. The true latitudes can be read from each curve at $\psi_{Limb} = 0$.

central meridian, $\psi_{Limb} = 90°$; however θ increases very slowly for high-latitude features which are never, of course, far from the limb.

Let us now recall that the contrast of a coronal feature with respect to the background intensity decreases as that feature is displaced from the limb; in Appendix A we argued that a typical coronal bright feature is visible when within about 35° from the limb. Thus many of the high apparent latitudes plotted in the top panel of Figure B2 apply to features so far from the limb as not to be visible. If we use this 35° estimate, the same calculation used to generate the bottom panel of the figure can be used to find the region of visible features in the top panel. Figure B3 shows this region on the plot of projected latitude versus longitude from the limb.

Figure B3 is the final result of this long discussion and the basis for the conclusions regarding the projected latitudes of coronal mass ejections, helmet streamers, or rays, already stated in the text. Features near the solar equator, or with small values of the true latitude λ, will be seen at projected latitudes Λ that are only slightly larger than λ; for such features the projection effect is significant only when they are so far from the limb to be seriously reduced in visibility. In contrast, high latitude features, are always near the limb (no farther than their colatitude) and can be seen at projected latitudes Λ significantly larger than λ. Under the $\theta \leq 35°$ criterion for visibility, a feature at a latitude $\lambda \geq 55°$ can be seen at any projected latitude Λ in the range from 55° to 90°. The magnitude of possible projection effects for intermediate cases can be read directly from Figure B3. It is of interest to note that virtually all of the small-scale activity during the SMM epoch (plotted on Figure 7) occurred within 40° of the solar equator. Typical coronal features extending radially outward from the extreme latitude, $\lambda = 40°$, would never be seen at projected latitudes greater than 52°.

These conclusions apply literally to an observer in the solar equatorial plane; they need only slight modification for the real case of an observer in the ecliptic plane which is tilted by 7 1/2° to the solar equator. The maximum modification is necessary at the two times in each year when the Earth (and observer) are at the maximum angle of 7 1/2° out of the solar equatorial plane, or at that angle above or below the x axis in Figure B1. In projection onto the plane of the sky, this places the radial line in that figure at an angle λ that is as much as 7 1/2° different from the true latitude. This difference is zero when that line is at the limb ($\psi = 90°$ or $\psi_{Limb} = 0°$), 7 1/2° when that line is at the central longitude $\psi = 0$ (or $\psi_{Limb} = 90°$). The effect on projected longitude Λ can then be visualized on Figure B3 by a new curve relating Λ to ψ_{Limb}, meeting the old curve at the limb, $\psi_{Limb} = 0$ and deviating from the old curve by 7 1/2° as $\psi_{Limb} \rightarrow 90°$. The modification for Λ is then only a few degrees for features at low or moderate latitudes when they are sufficiently close to the limb to be visible.

Acknowledgment. Major parts of the analysis described here were performed by J. T. Burkepile and O. C. St.Cyr. The author acknowledges discussions with and comments by R. R. Fisher, E. Hildner, R. A. Howard, D. F. Webb, and R. White on the material in this paper. The National Center for Atmospheric Research is sponsored by the National Science Foundation. The SMM observations and analysis reported here were funded under NASA contract S-04167D. I would also like to thank Liz Boyd for her incredible preparation of this manuscript.

The Editor thanks T. Forbes and A. Hewish for their assistance in evaluating this paper.

REFERENCES

Allen, C. W., *Astrophysical Quantities*, Athlone, London, 1973.

Billings, D. W., *A Guide to the Solar Corona*, Academic, San Diego, Calif., 1966.

d'Azambuja, M., and L. d'Azambuja, Etude d'ensemble des protuberances solaires et de leur evolution, *Ann. Obs. Paris, Sect. Meudon*, *6*(7), 1948.

Dryer, M., Coronal transient phenomena, *Space Sci. Rev.*, *33*, 233, 1982.

Fisher, R. R., Coronal mass ejection events, *Adv. Space Res.*, *4*(7), 163, 1984.

Fisher, R. R., C. J. Garcia, and P. Seagraves, On the coronal transient-eruptive prominence in 1980 August 5, *Astrophys. J.*, *246*, L161, 1981.

Forbes, T., Numerical simulation of a catastrophe model for coronal mass ejections, *J. Geophys. Res.*, *95*, 11,919, 1990.

Harrison, R. A., Solar coronal mass ejections and flares, *Astron. Astrophys.*, *162*, 283, 1986.

Harrison, R. A., The source regions of solar coronal mass ejections, *Sol. Phys.*, *126*, 185, 1990.

Harrison, R. A., Coronal transients and their relation to solar flares, *Adv. Space Res.*, *11*(1), 25, 1991*a*.

Harrison, R. A., Coronal mass ejection, *Philos. Trans. R. Soc. London, Ser. A*, *336*, 401, 1991*b*.

Harrison, R. A., E. Hildner, A. J. Hundhausen, D. G. Sime, The launch of solar coronal mass ejections: Results from the coronal mass ejection onset program, *J. Geophys. Res.*, *95*, 917, 1990.

Hewish, A., and S. Bravo, The sources of large-scale heliospheric disturbances, *Sol. Phys.*, *106*, 185, 1986.

Hewish, A., S. J. Tappin, and G. R. Gapper, The origin of strong interplanetary shocks, *Nature*, *314*, 137, 1985.

Hildner, E., Mass ejections from the corona into interplanetary space, in *Study of Travelling Interplanetary Phenomena*, edited by M. A. Shea, D. F. Smart, and S. T. Wu, p. 3, D. Reidel, Norwell, Mass., 1977.

Hildner, E., Do we understand coronal mass ejections yet?, *Adv. Space Res.*, *6*(6), 297, 1986.

Howard, R. A., N. R. Sheeley, Jr., M. J. Koomen, and D. J. Michels, Coronal mass ejections, 1979–1981, *J. Geophys. Res.*, *90*, 8173, 1985.

Howard, R. A., N. R. Sheeley, Jr., M. J. Koomen, and D. J. Michels, The solar cycle dependence of coronal mass ejections, in

The Sun and the Heliosphere in Three Dimensions, edited by R. G. Marsden, p. 107, D. Reidel, Norwell, Mass., 1986.

Hundhausen, A. J., An interplanetary view of coronal holes, in *Coronal Holes and High Speed Wind Streams*, edited by J. B. Zirker, pp. 225–329, Colorado Associated University Press, Boulder, 1977.

Hundhausen, A. J., The origin and propagation of coronal mass ejections, in Proceedings of the Sixth International Solar Wind Conference, edited by V. J. Pizzo, T. E. Holzer, and D. G. Sime, *Tech. Note NCAR/TN-306+Proc*, p. 181, Natl. Cent. for Atmos. Res., Boulder, Colo., 1987.

Hundhausen, A. J., R. T. Hansen, and S. F. Hansen, Coronal evolution during the sunspot cycle: Coronal holes observed with the Mauna Loa *K*-coronameters, *J. Geophys. Res.*, *86*, 2079, 1981.

Hundhausen, A. J., et al., Coronal transients and their interplanetary effects, in Solar Terrestrial Physics: Present and Future, edited by D. M. Butler and K. Papadopoulos, *NASA Ref. Publ.*, *1120*, pp. 6-1 to 6-32, 1984*a*.

Hundhausen, A. J., C. B. Sawyer, L. House, R.M.E. Illing, and W. J. Wagner, Coronal mass ejections observed during the Solar Maximum Mission: Latitude distribution and rate of occurrence, *J. Geophys. Res.*, *89*, 2639, 1984*b*.

Illing, R.M.E., and A. J. Hundhausen, Observation of a coronal transient from 1.2 to 6 solar radii, *J. Geophys. Res.*, *90*, 275, 1985.

Illing, R.M.E., and A. J. Hundhausen, Disruption of a coronal streamer by an eruptive prominence and a coronal mass ejection, *J. Geophys. Res.*, *91*, 10,951, 1986.

Kahler, S., Coronal mass ejections, *Rev. Geophys.*, *25*, 663, 1987*a*.

Kahler, S., Observations of coronal mass ejections near the Sun, in Proceedings of the Sixth International Solar Wind Conference, edited by V. J. Pizzo, T. E. Holzer, and D. G. Sime, *Tech. Note NCAR/TN-306+Proc*, p. 181, Natl. Cent. for Atmos. Res., Boulder, Colo., 1987*b*.

Kahler, S., R. L. Moore, S. R. Kane, and H. Zirin, Filament eruptions and the impulsive phase of solar flares, *Astrophys. J.*, *328*, 824, 1988.

Kiepenheuer, K. O., Solar activity, in *The Sun*, edited by G. P. Kuiper, pp. 322–465, University of Chicago Press, Chicago, Ill., 1953.

Klimchuk, J. A., Shear-induced inflation of coronal magnetic fields, *Astrophys. J.*, *354*, 745, 1990.

Low, B. C., Expulsion of magnetized plasmas from coronae, in *Solar Activity and Magnetic Fields: Origins and Coronal Effects*, edited by J. O. Stenflow, p. 467, D. Reidel, Norwell, Mass., 1983.

Low, B. C., Coronal mass ejections, in *Highlights of Astronomy*, edited by J.-P. Swings, p. 743, D. Reidel, Norwell, Mass., 1986.

Low, B. C., and A. J. Hundhausen, The velocity field of a coronal mass ejection: The event of September 1, 1980, *J. Geophys. Res.*, *92*, 2221, 1987.

Low, B. C., R. H. Munro, and R. R. Fisher, The initiation of a coronal transient, *Astrophys. J.*, *254*, 335, 1982.

MacQueen, R. M., Coronal transients: A summary, *Philos. Trans. R. Soc. London, Ser. A*, *297*, 605, 1980.

Martins, P.C.H., and N.P.M. Kuin, A circuit model for filament eruptions and two-ribbon flares, *Sol. Phys.*, *122*, 263, 1989.

Maunder, E. W., The Sun and sunspots, 1820–1920, *Mon. Not. R. Astron. Soc.*, *82*, 534, 1922.

Mihalov, J. D., A. Barnes, A. J. Hundhausen, and E. J. Smith, Solar wind and coronal structure near sunspot minimum: Pioneer and SMM observations from 1985–1987, *J. Geophys. Res.*, *95*, 8231, 1990.

Mikic, Z., D. C. Barnes, and D. D. Schnack, Dynamical evolution of a solar coronal magnetic field arcade, *Astrophys. J.*, *328*, 830, 1988.

Minneart, M., On the continuous spectrum of the corona and its interpretation, *Z. Astrophys.*, *1*, 209, 1930.

Munro, R. H., J. T. Gosling, E. Hildner, R. M. MacQueen, A. I. Poland, and C. L. Ross, The association of coronal mass ejection transients with other forms of solar activity, *Sol. Phys.*, *61*, 201, 1979.

Newkirk, G., Jr., Structure of the solar corona, Ann. Rev. Astron. Astrophys., *5*, 213, 1967.

Priest, E. R., Nonuniform magnetohydrodynamic nature of the solar corona, 1, Basic solutions, *Astrophys. J.*, *329*, 1009, 1988.

Rust, D. M., et al., Mass ejections, in *Solar Flares*, edited by P. A. Sturrock, p. 273, Colorado Associated University Press, Boulder, 1980.

Sheeley, N. R., Jr., R. A. Howard, M. J. Koomen, and D. J. Michels, Associations between coronal mass ejections and soft x-ray events, *Astrophys. J.*, *272*, 349, 1983.

Sheeley, N. R., Jr., R. A. Howard, M. J. Koomen, and D. J. Michels, Solwind observations of coronal mass ejections during 1979–1985, in Solar Flares and Coronal Physics Using P/OF as a Research Tool, edited by E. Tandberg-Hanssen, R. M. Wilson, and H. S. Hudson, *NASA Conf. Publ.*, *CP-2421*, 241, 1986.

St. Cyr, O. C., and J. T. Burkepile, A catalogue of mass ejections observed by the Solar Maximum Mission coronagraph, *Tech. Note NCAR/TN-352+STR*, Natl. Cent. for Atmos. Res., Boulder, Colo., 1990.

St. Cyr, O. C., and D. F. Webb, Activity associated with coronal mass ejections at solar minimum: SMM observations from 1984–1986, *Sol. Phys.*, 136, 379, 1991.

Steinolfson, R. S., MHD modeling of shear-induced coronal evolution and MHD shocks, in Max '91, Workshop #3, Max '91/SMM Solar Flares: Observations and Theory, edited by R. M. Winglee and A. L. Kiplinger, p. 123, Univ. of Colo., Boulder, 1990.

Steinolfson, R. S., Coronal evolution due to shear motion, *Astrophys. J.*, *382*, 677, 1991.

Sturrock, P. A., Maximum energy of semi-infinite magnetic field configurations, *Astrophys. J.*, *380*, 655, 1991.

Van de Hulst, H. C., The electron density of the solar corona, *Bull. Astron. Inst. Neth.*, *11*(410), 135, 1950.

Wagner, W. J., Coronal mass ejections, *Annu. Rev. Astron. Astrophys.*, *22*, 267, 1984.

Webb, D. F., The solar cycle variation of the rates of CMEs and related activity, *Adv. Space Res.*, *11*(1), 37, 1991.

Webb, D. F., and A. J. Hundhausen, Activity associated with the solar origin of coronal mass ejections, *Sol. Phys.*, *108*, 383, 1987.

Wolfson, R., Equilibria and stability of coronal magnetic arches, *Astrophys. J.*, *255*, 774, 1982.

Wolfson, R., Quasistatic evolution of coronal magnetostatic structures, in Coronal and Prominence Plasmas, edited by A. Poland, *NASA Conf. Proc.*, *CP-2442*, 269, 1986.

Wolfson, R., C. Conover, and R.M.E. Illing, The evolution of a coronal streamer prior to mass ejection, *J. Geophys. Res.*, *92*, 13,641, 1987.

A. J. Hundhausen, High Altitude Observatory, NCAR, M. S. 2920, Boulder, CO 80307.

(Received May 22, 1992;
revised January 5, 1993;
accepted January 6, 1993.)